The need for optoacoustic microscopy

Ludwig Englert

Institute of Biological and Medical Imaging,
Helmholtz Zentrum München,
Neuherberg, D-85764,
Germany
Chair of Biological Imaging at the Central Institute for Translational Cancer Research (TranslaTUM),
School of Medicine and Health,
Technical University of Munich,
Munich, D-81675,
Germany

Dominik Jüstel

Institute of Biological and Medical Imaging & Institute of Computational Biology,
Helmholtz Zentrum München,
Neuherberg, D-85764,
Germany
Chair of Biological Imaging at the Central Institute for Translational Cancer Research (TranslaTUM),
School of Medicine and Health,
Technical University of Munich,
Munich, D-81675,
Germany

Vasilis Ntziachristos*

Institute of Biological and Medical Imaging,
Helmholtz Zentrum München,
Neuherberg, D-85764,
Germany
Chair of Biological Imaging at the Central Institute for Translational Cancer Research (TranslaTUM),
School of Medicine and Health,
Technical University of Munich,
Munich, D-81675,
Germany

(Dated: October 29, 2024)

Optoacoustic (photoacoustic) microscopy resolves optical absorption in cells and tissues, thus offering a complementary contrast mechanism to optical microscopy. Yet, the marked advances in optical microscopy techniques and their widespread use beg the question on the particular need and utility of an additional microscopy modality that resolves optical absorption. We present recent advances that point to advantageous features and uses of optoacoustic microscopy in biological and clinical interrogation. We review how these advances can be manifested as part of hybrid implementations using optical, optoacoustic and possibly other forms of microscopy to enhance the ability of the microscopic interrogation. We further examine developments in the miniaturized optical detection of ultrasound, that can transform any optical microscope into a hybrid optical-optoacoustic system, and present recent progress with label-free molecular sensing and with new classes of novel reporters that expand the visualization capacity of the optoacoustic method. Finally, we discuss how hybrid optical-optoacoustic microscopy offers a next step in multimodal interrogations, impacting biological and clinical readings.

CONTENTS

* bioimaging.translatum@tum.de

I. INTRODUCTION

Optical microscopy spans 3.5 centuries of developments that have played a fundamental role in the progress of biology and the life sciences, enabling unprecedented insights into biological systems. Seminal advances over the last decades, including confocal (Davidovits and Egger, 1969), multiphoton (Denk *et al.*, 1990; Hellwarth and Christensen, 1974) and super-resolution microscopy (Bailey *et al.*, 1993; Heintzmann and Cremer, 1999; Rust *et al.*, 2006), and the introduction of fluorescent proteins (Chalfie *et al.*, 1994; Shimomura *et al.*, 1962), have tremendously expanded the use of the optical modality. A search in PubMed using the term "optical microscopy" reports more than 35,000 publications per year in the last few years, a marked and constant growth from ≈500 publications per year in the mid-1950's.

In the past few decades, the optoacoustic (OptA) method has received attention as a microscopy modality. While OptA approaches were first considered for gas sensing in the 1940's and 50's (Callisen, 1947; Delany, 1959), microscopy applications were described in the late 70's (Wong *et al.*, 1978) and 80's (Wada *et al.*, 1986, 1985). The term "*optical*", typically used for methods that use light for scientific measurements and imaging, is employed in many modalities such as *optical* microscopy, *optical* spectroscopy, *optical* coherence tomography, etc. (Ntziachristos, 2024). Similarly, the prefix "*opto*" in *opto*acoustics was initially employed in scientific publications (Callisen, 1947; Delany, 1959). Nevertheless, OptA microscopy (OptAM) is also broadly referred to as *photo*acoustic, i.e. photoacoustic microscopy (PAM) (Wang and Hu, 2012). Today, a search with the terms "optoacoustic microscopy" or "photoacoustic microscopy" reveals a volume of ∼150 publications per year. This number marks a significant growth of the modality since its initial introduction in the 1970's and 80's, and also indicates the challenges of adopting OptAM in biomedical applications. Indeed, inspection of this literature reveals publications that primarily drive the technology, rather than indicating a broad propagation of the method in the biomedical sciences.

The potential and challenges for a broad biomedical OptAM adoption can be explained by first describing its relation to the depth and the resolution that the method achieves in tissues (Fig.1). The OptA effect operates by converting light to ultrasound energy by means of thermo-elastic expansion. Briefly, chromophores that absorb light of transient energy (e.g. photon pulses) generate local volumetric expansions and contractions which give rise to ultrasound waves that are subsequently detected by ultrasound detectors (Delany, 1959; Jackson and Amer, 1980; Read, 1968; Rosencwaig, 1973). Consequently, the OptA method "listens" to light absorption in cells and tissues (Ntziachristos *et al.*, 2005), and then uses image formation techniques to generate images. Optoacoustics may be implemented to achieve microscopy resolutions using two approaches. The first is excitation with focused light, yielding images that obey optical diffraction principles. The second relates to employing broad illumination and recording frequencies at several tens of MHz and beyond, leading to images obeying ultrasound diffraction principles.

This second approach, the detection of optical contrast based on ultrasound diffraction, yields a fundamental advantage: images are formed without being significantly affected by photon scattering (Ntziachristos, 2010; Ntziachristos *et al.*, 2005; Wang and Hu, 2012). This feature enables the formation of high-resolution images in turbid media, deeper than optical microscopy, as originally described in the 80's and more thoroughly demonstrated in the 90's (Chen *et al.*, 1993; Kruger and Liu, 1994; Olsen and Lin, 1983). Since then, progress with powerful nanosecond lasers that can generate one cross-sectional image per single pulse, parallel detection of ultrasonic signals at the few MHz range and advanced model-based reconstruction methods (Taruttis and Ntziachristos, 2015) have allowed real-time OptA imaging at depths of at least a few centimeters in tissue, i.e. in the macroscopy range (see Fig.1a), for more than a decade now. OptA macroscopy typically operates in tandem with ultrasonography by means of using a common ultrasound detector for both modalities. The method has demonstrated broad imaging applications in humans, including imaging of breast cancer (Asao *et al.*, 2016; Diot *et al.*, 2017; Dogan *et al.*, 2019; Kukačka *et al.*, 2022; Oraevsky *et al.*, 2018; Zalev *et al.*, 2019), muscular dystrophy (Regensburger *et al.*, 2019),

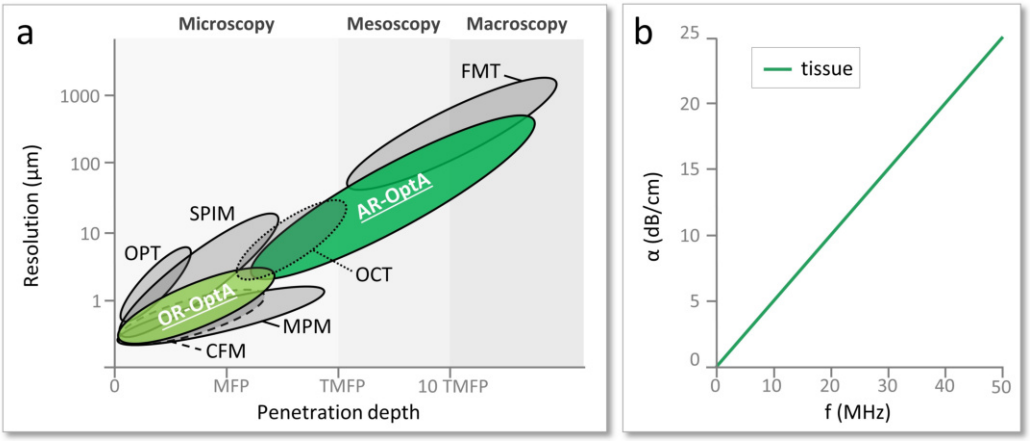

Figure 1 Resolution and penetration depth in optoacoustics. a) Comparison between common optical imaging technologies and optoacoustics with the penetration depth given as mean free path MFP and transport mean free path TMFP. OR-OptA optical-resolution optoacoustics, AR-OptA acoustic-resolution optoacoustics, CFM confocal fluorescence microscopy, MPM multiphoton microscopy, OCT optical coherence tomography, OPT optical projection tomography, SPIM selective plane illumination microscopy, FMT fluorescence molecular tomography (based on Ntziachristos 2010). b) Acoustic attenuation coefficient for tissue as a function of frequency (see equation 25 with $\alpha_0 \approx 0.5\text{dBMHz}^{-1}\text{cm}^{-1}$ and n ≈ 1; adapted from Deán-Ben *et al.* 2011).

metabolism and brown fat activation (Reber *et al.*, 2018), or the visualization of inflammation (Dogan *et al.*, 2019; Knieling *et al.*, 2017; Ntziachristos, 2024). Operation with ultra-wide bandwidths (few MHz to >100MHz) gives rise to optoacoustic mesoscopy (Omar *et al.*, 2019), which exchanges depth to resolution over macroscopy (see Fig.1a). OptA mesoscopy has enabled several clinical applications in monitoring dermatological and cardiometabolic conditions using the skin as a window to disease (Ntziachristos, 2024).

Nevertheless, as high ultrasound frequencies, at several tens of MHz and beyond, are utilized to match the resolution of optical microscopy, the OptAM depth also becomes similar to that of optical microscopy methods. The reason is that higher ultrasound frequencies experience steeper attenuation as a function of the distance that ultrasound propagates in tissues, compared to lower frequencies (see Fig.1b). Therefore, when using focused light beams or high ultrasound frequencies, OptAM generally operates within resolution and tissue penetration boundaries that match those of optical microscopy, as captured at the lower left corner of Fig.1a. Moreover, since hemoglobin is a common absorber of light in tissues, and concentrated in blood vessels, most OptAM works have focused on demonstrating imaging of tissue micro-vasculature or separating arterioles and venules in high resolution by resolving oxygenated and deoxygenated hemoglobin using multiple-wavelength illumination in the visible range (Kim *et al.*, 2019; Maslov *et al.*, 2005, 2008; Omar *et al.*, 2015; Ruan *et al.*, 2013; Seeger *et al.*, 2021; Wang and Hu, 2012; Zhang *et al.*, 2009). However, compared to the application profiles developed around optical microscopy, including fluorescence microscopy that utilizes contrasts that broadly reveal cellular and molecular structure and function, imaging micro-vasculature and micro-vascular oxygenation remains a very narrow target in biological interrogations. Initial efforts to identify genetic reporters for OptA contrast generation did not yield promising characteristics suited for broad OptAM adoption in biomedical communities. For example, fluorescent proteins have been resolved by OptA measurements (Märk *et al.*, 2017; Razansky *et al.*, 2009) but their absorption cross-sections and quantum yields have been optimized for fluorescence emission, and not OptA signal generation. Tyrosinase has also been considered as a reporter gene (Jathoul *et al.*, 2015; Stritzker *et al.*, 2013) to produce melanin, a strong light absorber, but the flat spectral response of melanin that lacks characteristic spectral features (peaks), and possible toxicity effects (Weissleder *et al.*, 1997) have limited tyrosinase applications. Therefore, despite the technological interest in OptAM, the method has faced challenges in relation to its use as a mainstream biological imaging modality.

The major aim of this review paper is to outline four technology and concept advances that have the potential to broadly propel OptAM adoption in the biomedical sciences. Advancements are required in

- hybrid optoacoustic implementations for multimodal interrogation, which employ OptAM modes to deliver enhanced biological information to the combined investigation.
- optical detection of ultrasound, which can seam-

lessly convert optical microscopes to hybrid optical-optoacoustic systems.

- the label-free OptA detection of molecules without needing external agents by using mid-infrared (mid-IR) illumination to significantly enhance the OptAM contrast.
- the development of new classes of photo-switching and bacterial reporters that can impart cellular and molecular contrasts to OptAM and OptA imaging.

Coupled with the use of three-dimensional point-spread functions for reaching theoretically predicted resolutions, this progress (Fig.3) can impart new abilities and serve as the basis for the wider dissemination of OptAM in the life sciences. In the following, we present the basis of OptA signal generation and propagation in tissues and describe the advances in the aforementioned emerging concepts and technologies and their relevance to introducing a number of new imaging modes not available to current optical methods. We outline examples of using these new modes in biological interrogations, explain how the described technologies can synergize to enhance the abilities of OptAM, and discuss their potential use in biomedical applications. Finally, we discuss the remaining limitations and give an outlook for the OptA modality.

II. THE OPTOACOUSTIC METHOD

A. Governing equations

Optoacoustic signal generation is based on the thermoelastic expansion of tissue structures that absorb light of transient intensity. This absorption of transient optical energy leads to a minute temperature increase and therefore a corresponding volumetric expansion and contraction, which generates a pressure wave. The propagation of this OptA pressure wave p in a homogenous medium can be expressed in terms of a thermoelastic wave equation

$$\ddot{p}(x,t) - v_s^2 \Delta p(x,t) = \frac{\beta}{\kappa} \ddot{T}(x,t), \tag{1}$$

where $x \in \mathbb{R}^3$ is the spatial variable, $t \in \mathbb{R}$ is the time variable, p is pressure, v_s is the speed of sound, β is the thermal coefficient of volume expansion, κ is the isothermal compressibility, and T is excess temperature, i.e., the temperature difference relative to the ambient temperature. For simplicity, we do at first not consider dispersive effects.

The dynamics of excess temperature are governed by the heat diffusion equation

$$\rho C_v \dot{T}(x,t) = k_{\text{th}} \Delta T(x,t) + H(x,t), \tag{2}$$

where ρ is mass density, C_v is specific heat capacity, k_{th} is thermal conductivity, and H is a heat source. In optoacoustics, the heat source is given by the heat generated by illumination with light

$$H(x,t) = \eta_{\text{th}} \mu_a(x) \varphi(x,t), \tag{3}$$

where η_{th} is the thermal conversion efficiency, μ_a is the absorption coefficient, and φ is fluence rate. We also introduce the total heat accumulated over time

$$H_{\text{tot}}(x) := \int_{\mathbb{R}} H(x,t')\mathrm{d}t' = \eta_{\text{th}} \mu_a(x) F(x), \tag{4}$$

where $F(x) := \int_{\mathbb{R}} \varphi(x,t')\mathrm{d}t'$ is fluence.

B. Thermal confinement

In most OptA implementations, temperature changes are induced by illuminating a target with short light pulses. The regime of thermal confinement is defined by a pulse width τ_L that satisfies $\tau_L \ll \tau_{\text{th}}$, where

$$\tau_{\text{th}} := \frac{d_c^2}{\alpha_{\text{th}}} \tag{5}$$

is the thermal relaxation time with d_c being the characteristic dimensions of the heated region, e.g. the diameter of a spherical region, and $\alpha_{\text{th}} = \frac{k_{\text{th}}}{\rho C_v}$ is thermal diffusivity. In such temporal confinement, the thermal diffusion term in eq. (2) does not significantly affect the temperature change in the heated region during the optical energy deposition and thus is negligible[1] (Kruger and Liu, 1994; Patel and Tam, 1981). On the timescale of the laser pulse, the effective dynamics reduce to $\rho C_v \dot{T}(x,t) = H(x,t)$. Plugging this equation into eq. (1), we get the OptA wave equation in the regime of thermal confinement, which is the commonly known wave equation in optoacoustics (Carome *et al.*, 1964; Rosencwaig and Gersho, 1976; Westervelt and Larson, 1973)

$$\ddot{p}(x,t) - v_s^2 \Delta p(x,t) = \Gamma \dot{H}(x,t), \tag{6}$$

where $\Gamma := \frac{\beta}{\kappa \rho C_v}$ is the Grüneisen coefficient.

[1] Formally, we can derive the dynamics in the limit $\frac{\tau_L}{\tau_{\text{th}}} \to 0$ by introducing a rescaled version of the heat source $H_\varepsilon(x,t) := \frac{1}{\varepsilon} H\left(x, \frac{t}{\varepsilon}\right)$, $\varepsilon > 0$, which satisfies $\int_{\mathbb{R}} H_\varepsilon(x,s)\mathrm{d}s = H_{\text{tot}}(x)$ for all $\varepsilon > 0$. On the time-scale of H_ε, eq. (2) becomes $\frac{\rho C_v}{\varepsilon} \dot{T}\left(x, \frac{t}{\varepsilon}\right) = k \Delta T\left(x, \frac{t}{\varepsilon}\right) + H_\varepsilon(x,t)$. Multiplying with ε and taking the limit $\varepsilon \to 0$, we arrive at the effective dynamics on the timescale of the laser pulse.

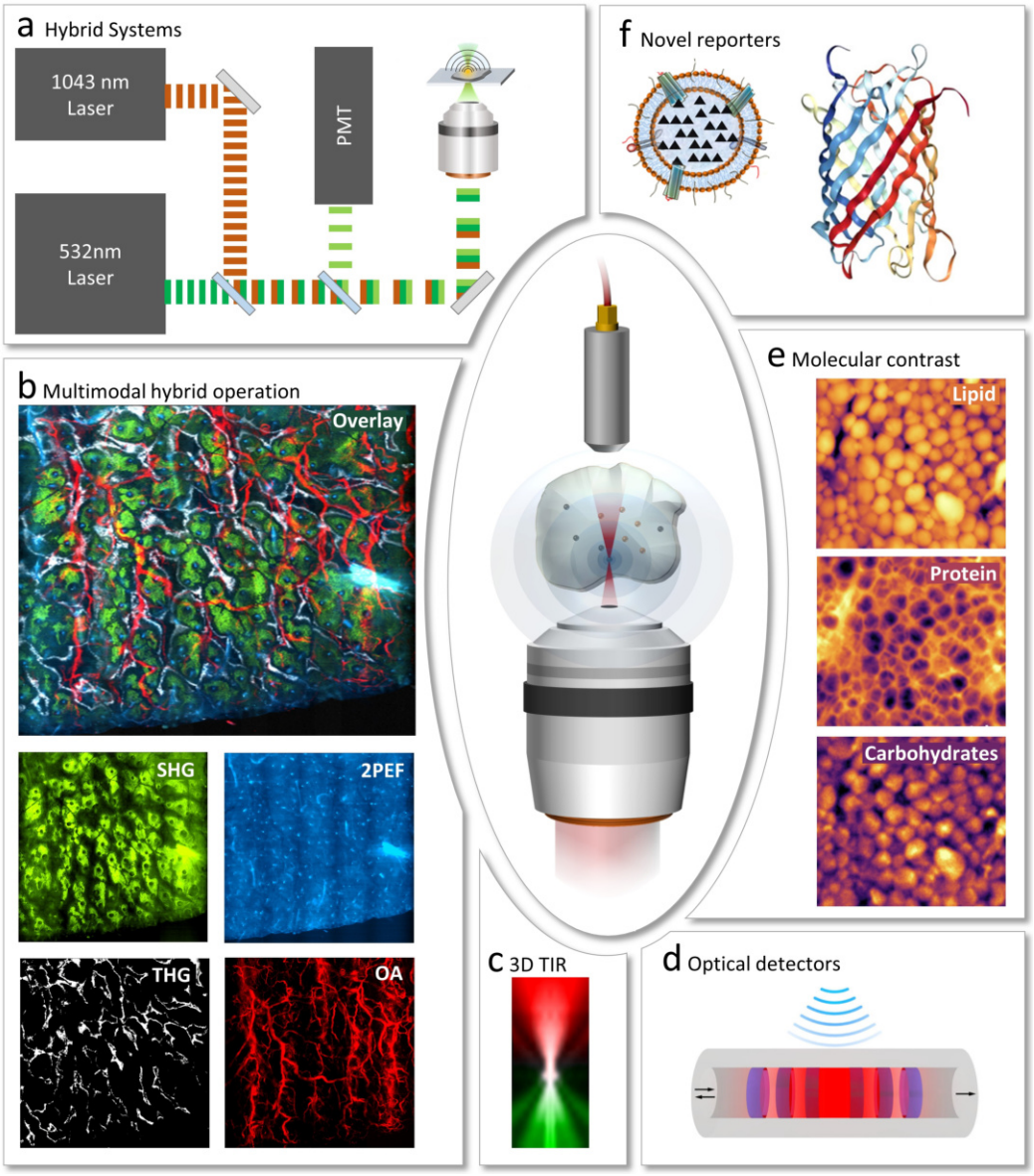

Figure 2 Key innovations for next generation optoacoustic microscopy (OptAM) in-particular: a) hybrid systems, b) multimodal hybrid operation (adapted from Seeger *et al.* 2021), c) point-spread-function (adapted from Seeger *et al.* 2020), d) new optical detectors Shnaiderman *et al.* 2017, e) label free molecular detection with mid-infrared OptAM (adapted from Pleitez *et al.* 2020) and f) reporter genes (adapted from Gujrati *et al.* 2019; Lei *et al.* 2020. PMT photomultiplier tube, SHG second-harmonic generation, THG third-harmonic generation, 2PEF two photon excitation fluorescence, OA Optoacoustic, TIR total impulse response.

C. Stress confinement

The regime of stress confinement (Oraevsky *et al.*, 1993) is defined by laser pulses that additionally satisfy $\tau_L \ll \tau_s$, where

$$\tau_s := \frac{d_c}{v_s} \tag{7}$$

is the stress relaxation time, which in this context describes the timescale of wave propagation. In this regime, pressure is induced by the short laser pulse on a time-scale much shorter than the time-scale of wave propagation.[2] The resulting equation is $\ddot{p}(x,t) = \Gamma \dot{H}(x,t)$ which can be integrated twice to get $p(x,t) = \Gamma \int_{-\infty}^{t} H(x,t')\mathrm{d}t'$. In other words, on this time-scale, the pressure rises with the induced heat. If the laser pulse is infinitely short, i.e.,

[2] Similar to the situation for thermal confinement, we can derive the dynamics in the limit $\frac{\tau_L}{\tau_s} \to 0$. The resulting equation is $\frac{1}{\varepsilon^2}\ddot{p}\left(x,\frac{t}{\varepsilon}\right) - v_s^2 \Delta p\left(x,\frac{t}{\varepsilon}\right) = \frac{\Gamma}{\varepsilon}\dot{H}_\varepsilon(x,t)$, which yields the reduced equation when multiplying with ε^2 and letting ε go to zero.

confined to $t = 0$, on the time-scale of wave propagation, then this situation intuitively results in an instantaneous initial pressure[3] $p_0 := p(\cdot, 0)$ equal to ΓH_{tot}. We confirm this intuition in the following by deriving the initial conditions on the timescale of wave propagation. Mild conditions on the laser pulse (e.g., finite duration is sufficient) imply that the rescaled heat source $H_\varepsilon(x,t) := \frac{1}{\varepsilon} H\left(x, \frac{t}{\varepsilon}\right)$ satisfies

$$\Gamma \dot{H}_\varepsilon(x,t) \rightharpoonup^*_{\varepsilon\to 0} \delta'(t)\Gamma H_{\text{tot}}(x) = \delta'(t)\Gamma\eta_{\text{th}}\mu_a(x)F(x) \quad \text{for all } x \in \mathbb{R}^3, \tag{8}$$

where δ' is the derivative of the Dirac delta.[4] The result is the source term formulation of the OptA wave equation in the regime of thermal and stress confinement

$$\ddot{p}(x,t) - v_s^2 \Delta p(x,t) = \delta'(t)\Gamma\eta_{\text{th}}\mu_a(x)F(x). \tag{9}$$

Infinitely short source terms induce instantaneous initial conditions. The derivative of the delta in time corresponds to an infinitely short velocity that is induced, leading to instantaneous initial values. As a consequence, the solution to the OptA wave equation (9) in stress confinement can be found by solving the initial value problem for $t \geq 0$

$$\begin{aligned} \ddot{p}(x,t) - v_s^2\Delta p(x,t) &= 0 \\ p_0(x) := p(x,0) &= \Gamma H_{\text{tot}}(x) = \Gamma\eta_{\text{th}}\mu_a(x)F(x) \\ \dot{p}(x,0) &= 0. \end{aligned} \tag{10}$$

D. Solution of the optoacoustic wave equation in thermal- and stress confinement

The general solution of the initial value problem introduced in eq. (10) is given by the following formula as an inverse Fourier transform

$$\begin{aligned} p(x,t) &= \frac{1}{(2\pi)^3}\int_{\mathbb{R}^3} \cos(v_s|k|t)\widehat{p_0}(k)e^{ik\cdot x}\mathrm{d}k \\ &= \mathcal{F}^{-1}\left[\cos(v_s|\cdot|t)\right] * p_0(x) =: G'_t * p_0(x), \end{aligned} \tag{11}$$

where the Fourier transform is defined as $\widehat{f}(k) := \mathcal{F}[f](k) := \int_{\mathbb{R}^d} f(x)e^{-ik\cdot x}\mathrm{d}x$, $*$ is convolution, and we introduced a variant of Green's function

$$G'_t(x) = \frac{\partial}{\partial t}\frac{1}{4\pi v_s^2 t}\delta\left(t - \frac{|x|}{v_s}\right), \tag{12}$$

for initial values, where the integration over the sphere is formally written as a delta distribution.[5] This variant is obtained by considering $\delta'(t)\delta(x)$ as source term.

We next consider the contribution of the initial pressure at a certain location x' by investigating the special case of a point-like absorber $\mu_a(x) = \mu_a(x')\delta(x - x')$. Noting that $v_s t = |x - x'|$ on that sphere, we obtain

$$p^\delta_{x'}(x,t) = \frac{\Gamma\eta_{\text{th}}\mu_a(x')F(x')}{4\pi v_s}\frac{\partial}{\partial t}\frac{\delta\left(t - \frac{|x-x'|}{v_s}\right)}{|x-x'|}, \tag{13}$$

which can be interpreted as radiated spherical pressure waves from an absorber point of view (Diebold *et al.*, 1991; Kruger and Liu, 1994; Wang and Wu, 2007; Westervelt and Larson, 1973). The usual expression for the full solution is obtained by integrating eq. (13) w.r.t. x'

$$p(x,t) = \frac{1}{4\pi v_s}\frac{\partial}{\partial t}\int_{S^2_{v_s t}(x)} \frac{\Gamma\eta_{\text{th}}\mu_a(x')F(x')}{|x-x'|}\mathrm{d}A(x'), \tag{14}$$

with $S^2_{v_s t}(x) := \{y \in \mathbb{R}^3 \,|\, |x-y| = v_s t\}$. This is Poisson's solution of the initial value problem (10) (Cox *et al.*, 2007). Eq. (14) may be interpreted as a detector obtaining pressure signals from sources carrying an initial pressure p_0 on a spherical shell centered around the observation point x with a radius of $v_s t$ as shown in Fig.3a.

E. Radially symmetric initial pressure

We investigate the special case of a radially symmetric initial pressure, i.e., the initial pressure p_0 satisfies $p_0(x) = p_0^{\text{rad}}(|x|)$, where we introduced the radial profile p_0^{rad} that uniquely defines p_0. This situation can occur, for example, if a radially symmetric absorber is illuminated homogeneously. As a consequence, the solution p is also radially symmetric, i.e., there is a function p^{rad} such that $p(x,t) = p^{\text{rad}}(|x|,t)$. Plugging this formula into eq. (11), and assuming that $p_0^{\text{rad}}(r) = 0$ for $r > R_s$, one obtains the following expression for p^{rad} after a short calculation

[3] Throughout these notes, we use dot-notation to indicate dependence on variables, e.g., if a function f depends on multiple variables, say $f(x,y,z)$, we write $f(x,\cdot,z)$ for the function that depends on y with fixed values for x and z.

[4] The derivative of the Dirac delta is the distribution that maps a test function to its derivative at zero, and $\rightharpoonup^*$ denotes weak-star convergence in the space of tempered distributions.

[5] Mathematically rigorous, G'_t is defined as the tempered distribution $G'_t = \frac{\partial}{\partial t}\frac{1}{4\pi v_s^2 t}\delta_{S^2_{v_s t}}$ with $\delta_{S^2_{v_s t}}(\varphi) := \int_{S^2_{v_s t}} \varphi(x)\mathrm{d}A(x)$ for $\varphi \in \mathcal{S}(\mathbb{R}^3)$, $S^2_{v_s t} := \{x \in \mathbb{R}^3 \,|\, |x| = v_s t\}$, where $\mathrm{d}A$ is the surface element, and $\mathcal{S}(\mathbb{R}^3)$ is the space of Schwartz functions on $\mathbb{R}^3$.

$$p^{\mathrm{rad}}(r,t) = \frac{1}{4\pi r}\int_0^\infty p_0^{\mathrm{rad}}(r')\left(\delta(r'+(v_s t-r))-\delta(r'-(v_s t-r))\right)r'\mathrm{d}r' \quad \text{for } t>0, \text{ and } r>R_s. \tag{15}$$

Introducing the profile of the radially symmetric initial pressure p_0^{profile} as the even extension of p_0^{rad}, i.e., $p_0^{\mathrm{profile}}(r) := p_0^{\mathrm{rad}}(|r|)$ for $r \in \mathbb{R}$, we observe that the above equation can be simplified to

$$p^{\mathrm{rad}}(r,t) = \frac{r-v_s t}{4\pi r}p_0^{\mathrm{profile}}(r-v_s t) \quad \text{for } t>0, \text{ and } r>R_s, \tag{16}$$

which, in case of a homogeneous radially symmetric initial pressure with radius R_s, yields the N-shape of the wave, since the profile is given by a rectangular pulse $p_0^{\mathrm{profile}}(r) = \mathrm{rect}(r/2R_s)$.[6] A physical interpretation of eq. (16) is to consider p_0 as the initial pressure inside the spherical absorber upon delta heating. The initial pressure is then distributed into two equal parts that initiate two spherical waves at the boundaries. The first wave travels away from the heated object as a diverging compression wave while the second wave travels inwards as a converging compression wave and becomes a diverging rarefaction wave after passing the center. The second wave then follows the first compression wave (Wang and Wu, 2007). The theory for a spherical absorber in a homogeneous medium has been experimentally confirmed in the early 1990s as shown in Fig.3b. The N-shaped pulse pattern in optoacoustics also occurs for example for a bursting balloon which presents an equivalent scenario – an initial pressure distribution in a spatially confined region (Deihl and Carlson, 1968; Diebold *et al.*, 1990; F. J. W. W, 1911).

The size of a homogeneous spherical absorber is inversely related to the frequency components of its OptA response, i.e., the bandwidth becomes wider for smaller absorbers. The Fourier transform of the N-shape $\widehat{N} := \mathcal{F}\left[p^{\mathrm{rad}}(r,\cdot)\right]$ is, up to a complex constant that depends on r, given by

$$\widehat{N}(\omega) \sim \frac{\left(\frac{\omega R_s}{v_s}\right)\cos\left(\frac{\omega R_s}{v_s}\right)-\sin\left(\frac{\omega R_s}{v_s}\right)}{\left(\frac{\omega R_s}{v_s}\right)^2}, \tag{17}$$

where $\omega = 2\pi f$ and the first maximum and -3dB cutoff frequencies are

$$f_{\max,1} \approx 0.33\frac{v_s}{R_s}, \quad f_{\mathrm{lower},1} \approx 0.16\frac{v_s}{R_s}, \quad \text{and} \quad f_{\mathrm{upper},1} \approx 0.51\frac{v_s}{R_s} \tag{18}$$

[6] With $\mathrm{rect}(r) = 1$ for $|r| \le \frac{1}{2}$ and $\mathrm{rect}(r) = 0$ for $|r| > \frac{1}{2}$.

(Oraevsky and Karabutov, 2000). For differently shaped absorbers, e.g., a cylinder or slab, but also for non-homogeneous mediums due to acoustic boundaries, different pulse shapes are obtained and, thus, the frequency components vary (Diebold *et al.*, 1991; Zuomin Zhao *et al.*, 1998).

F. System response

Transducer elements integrate the pressure over their surface. Let $E \subset \mathbb{R}^3$ be at the surface of the element. Integrating the response of a point source as given in eq. (13) yields the total pressure asserted by the point source $p_{x'}^{E,\delta}$:

$$p_{x'}^{E,\delta}(t) := \int_E p_{x'}^{\delta}(x,t)\mathrm{d}A(x) = \Gamma\eta_{\mathrm{th}}\mu_a(x')F(x')\frac{\partial}{\partial t}\frac{1}{v_s}\int_E \frac{\delta\left(t-\frac{|x-x'|}{v_s}\right)}{4\pi|x-x'|}\mathrm{d}A(x). \tag{19}$$

Introducing the spatial impulse response (SIR) $\mathrm{SIR}_{x'}^E$, and writing the time derivative as a convolution with the derivative of a delta, we get

$$p_{x'}^{E,\delta}(t) = \Gamma\eta_{\mathrm{th}}\mu_a(x')F(x')\delta' * \mathrm{SIR}_{x'}^E(t) \quad \text{with } \mathrm{SIR}_{x'}^E(t) := \frac{1}{v_s}\int_E \frac{\delta\left(t-\frac{|x-x'|}{v_s}\right)}{4\pi|x-x'|}\mathrm{d}A(x). \tag{20}$$

The definition of the SIR can be interpreted as the integration of pressure along the intersection of the detector element and the sphere of radius $v_s t$ around x'. The derivative of the delta can be interpreted as an infinitesimally short N-shape.

In addition, we introduce the electrical impulse response (EIR) of the transducer. Since we consider the system to be linear and time-invariant, the effect is fully described by convolution with a function EIR^E. The signal $s_{x'}^E$ acquired by the system is thus given by

$$s_{x'}^{E,\delta}(t) = \Gamma\eta_{\mathrm{th}}\mu_a(x')F(x')\delta' * \mathrm{SIR}_{x'}^E * \mathrm{EIR}^E(t). \tag{21}$$

Integrating over all source locations yields the full signal s^E recorded by the detector element:

$$s^E(t) := \int_{\mathbb{R}^3}\Gamma\eta_{\mathrm{th}}\mu_a(x)F(x)\delta' * \mathrm{SIR}_x^E * \mathrm{EIR}^E(t)\mathrm{d}x. \tag{22}$$

The electrical and spatial impulse responses are often combined in the so-called total impulse response (TIR) $\mathrm{TIR}_x^E := \mathrm{SIR}_x^E * \mathrm{EIR}^E$.[7]

[7] Eq. (21) simplifies to $s_{x'}^{E,\delta}(t) = \Gamma H_{\mathrm{tot}}(x')\frac{\partial}{\partial t}\mathrm{TIR}_x^E(t)$, i.e., measurements of signals generated by sub-resolution absorbers approximate the derivative of the TIR.

G. Detection limit

The detection of a pressure signal is limited by the presence of thermal noise. The minimally detectable pressure level for an ultrasonic detector is therefore usually given by the noise equivalent pressure (NEP) which is defined as

$$NEP(f) := \sqrt{\frac{k_B T[1+\frac{F_n}{\eta_{ac}(f)}]Z_a}{A}} \tag{23}$$

whereby k_B is the Boltzmann constant, F_n the amplifier's noise factor, $\eta_{ac}(f)$ the conversion efficiency from acoustic to electrical power at acoustic frequency f, Z_a the acoustic impedance of the coupling medium and A the area of the detector (Oraevsky and Karabutov, 2000; Winkler *et al.*, 2013). Considering a spherically focused piezoceramic detector operated in water (i.e. $Z_a \approx 1.5 \cdot 10^6 \mathrm{Pa{\cdot}s{\cdot}m^{-3}}$) at room temperature with a detection area A of $25\mathrm{mm}^2$, a focal distance L of 5mm, an efficiency η_{ac} of 0.001, which is assumed constant over the entire bandwidth $\Delta f = 50\mathrm{MHz}$, and an amplifier's noise factor $F_n \approx 2$ would result in a total NEP $\approx$ 5Pa if the frequency-dependent NEP is integrated over the detector's bandwidth. For a spherical droplet of hemoglobin in the focus ($\mu_a \approx 200\mathrm{cm}^{-1}$ and $\eta_{th} \approx 1$ at 532nm, with stress and thermal confinement being fulfilled) illuminated at a fluence F of $20\mathrm{mJ{\cdot}cm^{-2}}$, with Γ being 0.2 and the speed of sound v_s being $1450\mathrm{m}s^{-1}$ the NEP would limit the radius R_s of the droplet that could be detected to $\approx 0.8\mu$m according to eq. (16)[8] or $\approx 1.4\mu$m if acoustic attenuation is considered as well.

H. Acoustic attenuation

With the conversion from optical energy to acoustic energy the resulting pressure wave undergoes the laws of acoustic wave propagation and experiences attenuation in dispersive media. Dispersion and attenuation are captured by a dispersion relation that describes the relationship between frequency ω and wave vector k

$$k = \frac{\omega}{c(\omega)} - i\alpha(\omega). \tag{24}$$

For biological tissue, the acoustic attenuation coefficient is modeled as a power law in the frequency domain

$$\alpha(\omega) = \alpha_0 |\omega|^n, \tag{25}$$

with $n \approx 1$ and $\alpha_0 \approx 0.5\mathrm{dBMHz}^{-1}\mathrm{cm}^{-1}$ (Deán-Ben *et al.*, 2011; Duck, 1990). To describe dispersion and attenuation of acoustic signals, we consider these effects on a Dirac delta by integrating over all frequencies. The resulting function ATN captures both the broadening and the decay of the amplitude of a signal

$$\begin{aligned} \mathrm{ATN}(d,t) &:= \Re\left(\mathcal{F}^{-1}\left[e^{-ikd}\right](t)\right) \\ &= \Re\left(\frac{1}{2\pi}\int_{\mathbb{R}} e^{\left(-i\frac{\omega}{c(\omega)}-\alpha(\omega)\right)d} e^{i\omega t}\mathrm{d}\omega\right), \end{aligned} \tag{26}$$

where $\Re(z)$ denotes the real part of a complex number $z \in \mathbb{C}$ and d the distance over which the effect is introduced. While it seems plausible to add this filter ATN to eq. (22) to include the dispersive effects, it is instead necessary to formulate the dispersive wave equation defined by the dispersion relation (24) and derive its solution (see Treeby and Cox 2009), which goes beyond the scope of this paper as all introduced equations in this chapter would change.

I. Optoacoustic image reconstruction

Optoacoustic image reconstruction aims to obtain the initial pressure distribution, given the measured OptA signals. According to eq. (14), the pressure wave p measured by a detector placed at location x and time t has potentially been generated at any point on the spherical surface with radius $v_s t$ centered at the detector's position. Reconstruction algorithms intend to find the correct distribution of absorbers, using measurements of p at multiple detector locations to overcome this ambiguity.

Although the field of reconstruction in OptA is wide, it is useful to differentiate two major and common approaches (Lutzweiler and Razansky, 2013; Omar *et al.*, 2019). The first approach relates to back-projection formulas (Andreev *et al.*, 2002; Xu and Wang, 2005), which are analytic solutions of the inverse problem in a setting with multiple simplifying assumptions (e.g., point detectors, full angular coverage). In this situation, the initial pressure is uniquely determined by the signals and recovered via the following formula that is correct for the three common geometries (planar, cylindrical, and spherical detection):

$$p_0(x) = \frac{1}{\Omega_0}\int_{S_0} b\left(x', \frac{|x-x'|}{v_s}\right)\mathrm{d}\Omega_0(x', x), \tag{27}$$

where $b(x,t) := 2p(x,t) - 2t\dot{p}(x,t)$,

$$\mathrm{d}\Omega_0(x', x) := n_{S_0}(x') \cdot \frac{(x-x')}{|x-x'|}\frac{\mathrm{d}A(x')}{|x-x'|^2} \tag{28}$$

is the contribution of the detection surface element to the reconstruction, and Ω_0 is the solid angle of the

[8] The initial pressure p_0 is calculated via eq. (10), while the peak pressure of the N-shape at a distance L is given by eq. (16). Note that the solid angle is already considered in the definition of NEP by the surface A.

detector array (i.e., $\Omega_0 = 2\pi$ for the planar geometry, $\Omega_0 = 4\pi$ for the spherical and cylindrical geometries), S_0 is the detection surface, and $n_{S_0}(x')$ is the surface normal at $x' \in S_0$ pointing towards the source (Xu and Wang, 2005). The reconstruction can be interpreted as the projection of the term $b(x,t)$ that depends on the observed OptA signals p via a spherical surface centered at the observation point x. This reconstruction formula is intimately related to the inverse spherical radon transformation (Kunyansky, 2007; Lutzweiler and Razansky, 2013; Wang and Wu, 2007). Due to its computational efficiency, backprojection is often used even if the underlying assumptions are violated, resulting in image artefacts.

The second approach is called model-based reconstruction (Paltauf *et al.*, 2002). In this approach, the reconstruction is reformulated as an optimization problem of the following form

$$p_0^* := \arg\min_{p_0} \|Mp_0 - s\|^2 + \lambda\Omega(p_0), \tag{29}$$

where p_0^* is the reconstructed initial pressure distribution, M is the matrix that represents the linear forward model (e.g., as given in eq. (22)) in a chosen basis, s is the measured signal, λ is the regularization parameter, and Ω is the regularization functional. In other words, the model-based approach finds the initial pressure distribution with the following property: If the forward model is applied to the initial pressure distribution, the resulting sinogram is as close to the measured sinogram as possible.

The optimization problem (29) is usually solved with iterative methods (Deán-Ben and Razansky, 2022; Laufer *et al.*, 2010; Omar *et al.*, 2019; Rosenthal *et al.*, 2011b), which are notoriously slow. The model-based approach allows the integration of specific details of the imaging system into the image reconstruction via the model matrix, and to counteract the ill-posedness of the reconstruction problem via the regularization. Consequently, model-based inversion leads to a higher fidelity reconstruction and quantification over back-projection methods. The requirement for reconstruction depends on the implementation of the imaging system and is usually anticipated for tomography setups.

III. OPTOACOUSTIC MODES OF OPERATION

The two fundamental implementations of OptAM, briefly mentioned in the introduction, are shown in (Fig.4a and b). The implementation which uses focused light, first described in the late 70's (Wong *et al.*, 1978), can be referred to as optical-resolution (OR) OptAM. The method is generally limited to sub-1mm depths by photon scattering and resolution limited by optical diffraction in ways similar to optical microscopy (Ntziachristos, 2010; Wang and Hu, 2012). The second implementation, which uses non-focused, broad beam light illumination, results in image formation and resolution that is based on the characteristics of the ultrasound detector employed and ultimately limited by ultrasound diffraction (Chen *et al.*, 1993; Olsen and Lin, 1983). This implementation is also referred to as acoustic resolution (AR) OptAM. Detection bandwidths of 20-40MHz with central frequencies in the few tens of MHz lead to resolutions of ∼20-30μm (Laufer *et al.*, 2012; Zhang *et al.*, 2006), whereby bandwidths of >100MHz at central frequencies of several tens of MHz or higher allow resolutions within the sub-10 micrometer range (Aguirre *et al.*, 2017), at more superficial depths. The depth vs. resolution exchange depends on both the optical and ultrasound attenuation. Generally, the optical attenuation is steeper than the ultrasound attenuation for frequencies of a few tens of MHz. Therefore, the selection of wavelength dictates the depth reached by OptA macroscopy and mesoscopy. Conversely, for OptA microscopy, ultrasound attenuation contributes to the overall attenuation of the OptA signal and may become the main attenuation factor for several tens of MHz and higher, limiting the depth achieved. Consequently, resolutions of up to 1.3μm have been shown at the 1GHz frequency range, albeit only for *in-vitro* imaging of cells (Strohm *et al.*, 2013).

OR-OptAM and AR-OptAM can be implemented in epi-illumination or transmission modes (Fig.4c and d), and have been extensively employed to visualize microvasculature, based on the absorption of hemoglobin (Aguirre *et al.*, 2018; He *et al.*, 2022; Kim *et al.*, 2016, 2019; Liao *et al.*, 2010; Maslov *et al.*, 2008; Omar *et al.*, 2015; Ruan *et al.*, 2013; Schwarz *et al.*, 2016; Seeger *et al.*, 2021; Zhang *et al.*, 2009, 2006). Hemoglobin is a natural tissue photon absorber that is concentrated in blood vessels, giving rise to strong OptA signals and allowing label-free visualization of microvasculature with high contrast. It has been shown that single red blood cell resolution can be achieved in OR-OptAM mode (Seeger *et al.*, 2020; Strohm *et al.*, 2013; Wang *et al.*, 2013). Moreover, since the absorption spectra between its oxygenated and deoxygenated forms are different, it is possible to differentiate oxy- from deoxy-hemoglobin when using illumination at multiple wavelengths (Schwarz *et al.*, 2016). Other endogenous tissue chromophores have also been visualized in exploratory studies by OptAM. Melanin is another naturally occurring strong optical absorber and has been used as endogenous contrast for cell imaging *in-vitro* (Strohm *et al.*, 2013), visualization of melanocyte populations in zebrafish larvae *ex-vivo* (Tserevelakis *et al.*, 2014), melanophore migration in developing zebrafish *in-vivo*,

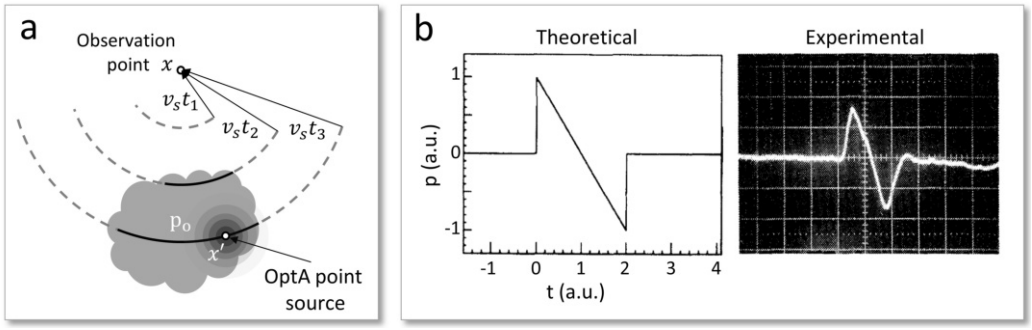

Figure 3 OptA in Theory. a) The forward solution in eq. (14) can be considered as a spherical shells with radius $v_s t$ centered at an observation point x. Once the shell intersects the arbitrary shaped source an OptA signal is obtained at the observation point. A particular optoacoustic point source is depicted at x'. b) N-shape like signal as the theoretical solution for a spherical absorber in a homogenous medium (left) and experimentally derived N-shape like signal generated from a benzaldehyde droplet suspended in water (adapted from Diebold *et al.* 1991).

(Kneipp *et al.*, 2015) or visualization of laser-induced retinal injury and neovascularization in the rat retina *in-vivo* (Xiao *et al.*, 2020). Neuromelanin can also be used as an endogenous absorber and has been visualized in intact human midbrain organoids (Englert *et al.*, 2023). Cytochrome C has offered OptA contrast in differentiating cytoplasm and nuclei in fixed fibroblasts (Zhang *et al.*, 2013) and HeLa live cell cultures (Haven *et al.*, 2020). Imaging in the ultraviolet (UV) range has enabled label-free visualization of DNA/RNA at epithelial cell nuclei of a mouse ear (Yao *et al.*, 2010) and adipose tissue (Bell *et al.*, 2021). In two studies, myoglobin, a protein mainly present in muscles and involved in oxygen transport, has also been imaged *ex-vivo* to reveal myocardial sheet architecture in excised dog tissue (Zhang *et al.*, 2012a) or its bio-distribution in rat muscles as in the stomach and heart (Sun *et al.*, 2020).

While these studies have demonstrated the basic principles of OptAM, they only offer a small set of niche applications compared to the operation modes and contrast available in optical microscopy, which is capable of visualizing complex functions at multiple levels of cellular organization and function. However, key advances over the past decade have the potential to expand the utility and applications of OptAM, addressing a larger number of biological and possibly medical imaging applications, as summarized in the following.

IV. HYBRID OPTOACOUSTIC MICROSCOPY

The OptA method offers two compelling advantages over the optical method. First, when applied in AR mode, it can visualize deeper than optical microscopy and therefore extend the scale of visualization. As depth increases, the resolution decreases, but in contrast to optical methods, it retains ability to form high-resolution images; for example, resolutions in the tens of microns through several millimeters of tissue (Ntziachristos, 2010). Second, OptA detection resolves light absorption, as opposed to fluorescence or other contrast mechanisms. Therefore, it can visualize endogenous absorbers (see Section VII) or novel reporters for contrast generation (see Section VIII) complementing structural and functional observations of optical methods. However, since optical microscopy is already very advanced and can reveal a very broad range of biological targets, well beyond the contrast achieved so far by OptAM, adoption of OptA microscopy in biomedical applications requires the identification of clearly established application advantages offered by the OptA mode.

In this vein, a major recent drive for considering the OptA method in biological imaging is its combination with established microscopy techniques in hybrid implementations. Recent progress with optical detection of sound (see Section V) can be combined with inexpensive sources (see Stylogiannis *et al.* 2022) to offer the potential for a seamless and economic integration, opening up the possibility for synergy between the two modalities. Different modes of hybrid integration lead to particular advantages. For example, the combination of optical microscopy with OR-OptAM generally operates on the same resolution and depth specifications but can enhance optical contrast with OptA detection modes, for example label-free detection of molecules (see Section VII). Critically, integration with AR-OptAM is a strategy that can extend the penetration depth over optical microscopy. However, this advantage becomes particularly relevant when the contrast visualized by the two methods is of biological interest. For example, interest to visualize a particular cell function on the optical mode using fluorescent labels may not be compatible with visualizing microvasculature, deeper in tissue, offered by AR-OptAM contrast. This interplay with physical performance and biological contrast is of

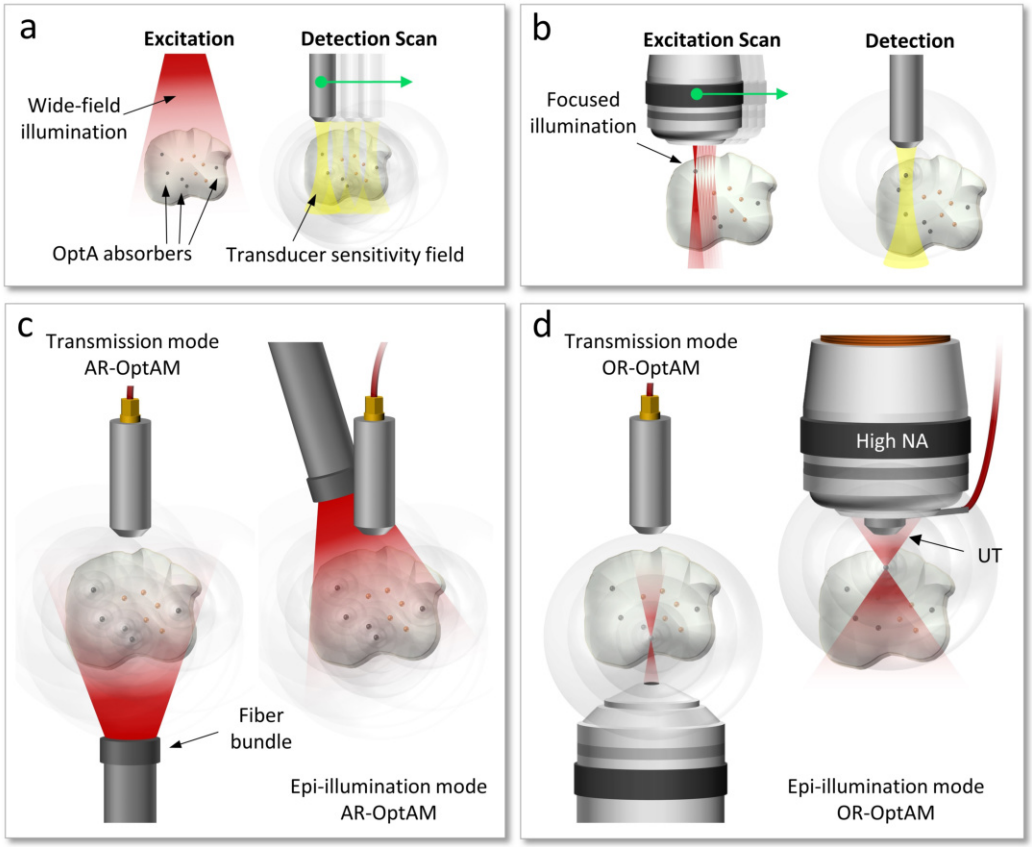

Figure 4 Optoacoustic principle with acoustic-resolution optoacoustic microscopy (AR-OptAM) and optical-resolution optoacoustic microscopy (OR-OptAM) in transmission and epi-illumination mode. a) AR-OptAM employs wide-field illumination and generates optoacoustic signals from multiple absorbers over the illuminated volume. The signals are detected using a detector which scans over the area of interest. Multiple stationary or scanning detectors can be also used. Image formation may then use mathematical inversion. b) OR-OptAM scans focused illumination to generate optoacoustic signals primarily from the optical focus. Image formation can then be based on appending consecutive scans acquired by the ultrasound detector (UT). Depth selection, at the focal point, can be achieved by time-gating the optoacoustic signal collected. c) AR-OptAM with a fiber bundle delivering wide-field illumination to the sample in transmission and epi-illumination mode. d) OR-OptAM with an objective lens focusing the beam in the transmission mode implementation while, in the epi-illumination mode implementation, a high numerical aperture (NA) objective lens focuses the light with the ultrasound detector being placed centrally below the objective lens output's optical aperture on an optical window connected via a small bridge.

key importance for the adoption of OptA microscopy in biological sciences (see discussion in Section X). In addition, OptA microscopy modes can be also combined with other microscopy methods, such as ultrasound microscopy.

In the following we review progress with hybrid OptA systems and the complementary achieved in contrast. Tables I – III summarize technical and imaging performance specifications, modes of operation, and application on hybrid systems.

A. Hybrid optoacoustic and nonlinear/confocal/light sheet microscopy

Confocal or two-/multi-photon microscopy utilizes techniques that reduce the sensitivity of conventional optical microscopy to scattering and enable optical diffraction-limited visualization at several tens to hundreds of micrometers under the tissue surface, an ability also referred to as optical tissue sectioning. These microscopy methods are well suited for hybrid implementations with OptAM, since they match the operational OptAM characteristics. Two photon excitation fluorescence (2PEF) and three photon excitation fluorescence (3PEF) microscopy generally penetrate deeper into tissues (∼0.5 – 1 mm) than confocal fluorescence microscopy (CFM: 0.1-0.2 mm) and may be better suited for OptAM hybrid implementations. Nevertheless, all

combinations have been explored and showcase the value in contrast enhancement by hybrid operation.

Hybrid multi-photon and OptAM setups have been considered for visualizing optical and OptA contrast *in-vivo* and *ex-vivo* (Rao *et al.*, 2014; Seeger *et al.*, 2021, 2016, 2019; Soliman *et al.*, 2015a,b; Song *et al.*, 2016; Tserevelakis *et al.*, 2014). A first hybrid implementation demonstrated up to 6-modal operation (see Table I) by employing conventional bright-field microscopy, a femtosecond laser source for 2PEF, second-harmonic generation (SHG) and third-harmonic generation (THG) contrast and a nanosecond laser for OR- and AR-OptAM capturing of absorption contrast. The method was applied to revealing structural and functional features *in-vivo* in mice and in zebrafish larva associated with anatomical features or to revealing the spatiotemporal tissue reorganization over 68 days of wound healing (Seeger *et al.*, 2021, 2019; Soliman *et al.*, 2015b; Tserevelakis *et al.*, 2014). Contrast has been obtained from elastin and hair follicles by two-photon excitation fluorescence (2PEF) microscopy, collagen (SHG), lipid accumulations predominantly in sebaceous glands (THG), and microvasculature due to hemoglobin (OptAM) while an additional bright-field (BF) channel provided orientation on the tissue (Seeger *et al.*, 2021, 2019) (Fig.5a). Furthermore, contrast from melanin has been obtained with the OptAM channel in zebrafish larvae (Tserevelakis *et al.*, 2014). Hybrid investigation of carotid atheroma *ex-vivo* also revealed co-registered differences from collagen, elastin and red blood cells from healthy and atheromatous tissue without the need for multiple staining (Seeger *et al.*, 2016). Hybrid dynamic imaging of cardiac organoids at 1Hz has also been demonstrated using an OptA calcium sensor (Roberts *et al.*, 2018).

Similar implementations of nonlinear microscopy and OptAM (see Table I) were used to generate high-resolution images in the sub-micron range of an *in-vivo* mouse ear in full reflection mode (Song *et al.*, 2016). Autofluorescence from nicotinamide adenine dinucleotide (NADH), an enzyme related to redox metabolism, and collagen (SHG) were used to visualize cells and hair shafts, whereby hemoglobin contrast revealed the mouse ear vasculature by OptAM. Furthermore, using a cranial window to expose the cortex, OptAM visualized the cortical vasculature and fine neural microstructures including dendrites and cell bodies based on contrast from the Green Fluorescent Protein (GFP) captured with 2PEF in a thy1-GFP mouse *in-vivo*. These applications demonstrated complementary readouts between OptAM and autofluorescence or GFP-expressing structures, enabling broader understanding of tissue microarchitecture in living animals.

Confocal microscopy, based on continuous wave (CW) light sources, has also been used in hybrid implementations with OptAM to visualize human and animal eye morphology and function (Tserevelakis *et al.*, 2017, 2020, 2022, 2016; Wang *et al.*, 2011; Yu Wang *et al.*, 2010; Zhang *et al.*, 2010a,b, 2011). Contrast from autofluorescent lipofuscin in the retinal pigment epithelium resolved by CFM and melanin in the choroid, i.e., the vascular layer of the eye, was resolved by OptAM was applied to reveal age-related macular degeneration (Zhang *et al.*, 2010b). In a similar study, OptAM (melanin) and CFM (tissue autofluorescence from collagen, elastin etc.) differentiated nevi and melanomas in human conjunctival nevus ocular biopsies from patients (Tserevelakis *et al.*, 2020). An OptAM-CFM implementation with a single shared tunable laser source was also shown to visualize morphological and functional features of blood and lymphatic vessels in mouse ears, *in-vivo* (Yu Wang *et al.*, 2010). OptAM images at two different wavelengths resolved the vasculature system and hemoglobin oxygen saturation (sO_2) maps. The CFM channel was used to image the lymphatic network using a Rhodamin-B-Isothiocyanat-dextran dye. In a subsequent study (Wang *et al.*, 2011), the system was used to assess the hemoglobin oxygen saturation and oxygen partial pressure in mouse ears. For validation of the OptAM readings, an oxygen sensitive phosphorescent probe was injected into the vasculature and excited at 532nm to sense the oxygen partial pressure pO_2 via the phosphorescence lifetime using the CFM channel. Separation of sebaceous glands from blood vasculature was based on temporally modulating the induced phosphorescence signals over the autofluorescence signal.

A combination of OptAM together with CFM and 2PEF has also been investigated (Rao *et al.*, 2014) in moss leaves and showcased the collection of 2PEF signals from leaf cell boundaries and chloroplasts inside leaf cells, using autofluorescence from chloroplasts collected with CFM and background absorption signals recorded by OptAM. Using only the CFM and OptAM modes, this system was also employed to image the sectioned retina of a transgenic mouse *ex-vivo*, whereby CFM resolved autofluorescence from photoreceptor cells and yellow fluorescent protein expressing labeled bipolar cells while OptAM imaged the retinal pigmented epithelium layer. CFM and OptAM also visualized the ventral tract of the spinal cord, the posterior lateral line nerve, bright interneuron-like cells (CFM) and skin melanin content and vasculature (OptAM) in the skin of zebrafish embryo.

The combination of hybrid OptA and selective plane illumination microscopy (SPIM), also known as light sheet microscopy (LSM), has also allowed imaging zebrafish development during stages not possible by purely optical methods. Using a single common illumination source, a

hybrid OptA-SPIM system (Lin *et al.*, 2015) was shown to resolve melanocytes and morphology based on other naturally occurring chromophores (OptAM), autofluorescence from muscle fibers and ganglions and GFP-expressing afferent neurons around the head (SPIM). This implementation emphasizes the use of OptA to reach deeper in tissue and visualize in the presence of strong photon-scattering, enabling zebrafish imaging over development times of several weeks, whereby the fish transform from early-stage transparent organisms into their adult opaque appearance, a process not possible to image by SPIM. Therefore, the hybrid OptA/SPIM system has become the first system to continuously visualize zebrafish development from early stages to adulthood, capturing up to 6 weeks of development (Vetschera *et al.*, 2023). Using multi-wavelength illumination and spectral unmixing techniques, visualization of lipids, melanin and hemoglobin has also been shown to be possible in live zebrafish (Vetschera *et al.*, 2023).

B. Hybrid optoacoustic and optical coherence tomography

OptAM and optical coherence tomography (OCT) also share optical tissue sectioning abilities and can capitalize on the complementary contrast offered. OCT primarily reveals morphological contrast based on photons backscattered from tissue micro-interfaces at different depths (Aumann *et al.*, 2019) and may reach depths beyond 1mm, depending on the amount of scatter present in tissue. This scattering contrast is well complemented by OptA contrast, in particular as provided by ultra-broadband OptA mesoscopy (Omar *et al.*, 2019). Operating at bandwidths of several tens of MHz, up to 100Mhz, OptA offers resolutions that are similar to the ones achieved by OCT, while extending the contrast visualized to absorption-based morphology, functional and molecular detection. Proof-of-principle demonstrations on mouse ears and ophthalmic applications have been shown with a multitude of systems (Bondu *et al.*, 2018; Dadkhah and Jiao, 2020; Dadkhah *et al.*, 2019; Jiao *et al.*, 2009; Lee *et al.*, 2013; Liu *et al.*, 2015, 2016; Song *et al.*, 2014; Zhang *et al.*, 2018, 2012c, 2011). A first implementation, based on Doppler spectral domain OCT (SD-OCT) combined with OptAM, assessed the retinal metabolic rate of oxygen of rats (Song *et al.*, 2014) (Song et al. 2014). Multispectral OptAM evaluated the retinal sO_2 of individual vessels of a rat's eye while Doppler SD-OCT analyzed the retinal flow in the vessels. Sensing of sO_2 and blood flow enabled assessment of the retinal oxygen metabolic rate $rMRO_2$ in a label-free non-invasive manner. A more advanced system combining OptAM, fluorescence microscopy (FM) and OCT was developed to assess retinal neovascularization (RNV), an abnormal growth of blood vessels in the retina associated with numerous ophthalmic diseases, representing a major cause of vision loss and blindness (Zhang *et al.*, 2018). The system has been used to visualize RNV in albino and pigmented rabbits *in-vivo*. RNV was triggered in living rabbits and compared to normal rabbits after 7 days based on OptAM, FM and OCT. OptAM and color fundus images revealed a significant increase in the tortuosity and numerous new tortuous angiogenetic vessels grown over the retina for the RNV group. Fluorescein sodium-induced fluorescence images corroborated the OptAM and color fundus findings, whereby OCT provided cross sections of the different retinal layers. A further combination of OCT, OCT angiography (OCTA), CFM and OptAM has been demonstrated in a single setup to assess complementary information of the vasculature in small animals (Dadkhah and Jiao, 2020). OptAM was used to visualize the vasculature network of a mouse ear *in-vivo*, while CFM revealed the autofluorescence of the tissue, OCT revealed the general tissue structure, and OCTA added the ability to assess blood flow in the vessels, thus complementing the study of functional microvasculature characteristics with a potential use in retinal imaging for the study and diagnosis of degenerative retinal diseases (Fig.5b).

C. Hybrid optoacoustic and ultrasonography implementations

Hybrid implementations involving ultrasonography (US) and OptAM are relatively straightforward, as they can use the same ultrasound element for implementing both modalities. Nevertheless, a hybrid system requires implementation of timing and appropriate electronics that separate ultrasound emission from ultrasound and OptA detection. Hybrid US and OptA systems have been demonstrated both for AR-OptAM (Harrison *et al.*, 2009; Jiang *et al.*, 2010; Subochev *et al.*, 2012, 2015) and OR-OptAM (Dai *et al.*, 2015; Estrada *et al.*, 2020; Rebling *et al.*, 2018; Strohm *et al.*, 2013, 2016) combining contrast from light absorption (OptAM) and tissue acoustic impedance mismatches (US). Cranial bone anatomy of mice *in-vivo* has been visualized by US, whereby cerebral vascular networks were co-registered based on OptAM contrast (Rebling *et al.*, 2018). Additionally, by using optically fast switching between two wavelengths, OptAM visualized blood oxygenation in the vessels of the murine brain (Fig.5c). Besides providing anatomical images of the cranial bone, US was employed in a subsequent study to assist in OptAM image segmentation and to differentiate between calvarian vasculature and vasculature of the brain (Estrada *et al.*, 2020). The combination of functional and anatomical readouts offer assessments of healthy and pathological neurovasculature in a label-free and non-invasive manner. High frequency US and hybrid OR/AR-OptAM was also combined in a single setup developed to image single cells

Table I Optoacoustic techniques with nonlinear, confocal and light sheet microscopy. AR-OptAM acoustic resolution optoacoustic microscopy, OR-OptAM optical resolution optoacoustic microscopy, (T) transmission mode, (R) reflection mode, MPM multiphoton microscopy, SHG second-harmonic generation, THG third-harmonic generation, 2PEF 2-photon excitation fluorescence, OCT optical coherence tomography, CFM confocal microscopy, SPIM selective plane illumination microscopy, BF bright-field, GFP green fluorescent protein, NADH Nicotinamide adenine dinucleotide.

System overview	Mode	Wavelength (nm)	Contrast	Resolution lateral (µm)	Resolution axial (µm)	Applications	References
6-modes AR-OptAM + OR-OptAM + SHG + THG + 2PEF + BF	OR- OptAM (T)	532	Hemoglobin, Melanin	0.4	6	Zebrafish larva morphology (*ex-vivo*)	Tserevelakis *et al.*, 2014; Soliman *et al.*, 2015a; Soliman *et al.*, 2015b; Seeger *et al.*, 2016; Seeger *et al.*, 2021
	AR- OptAM (T)	532	Hemoglobin, Melanin	20	6	Mouse ear wound healing (*in-vivo*)	
	MPM (T+R)	1043	Collagen, Lipids, Elastin	0.7	6	Spatiotemporal distribution of calcium in heart organoid (*in-vitro*)	
						Human carotid atheroma morphology	
3-modes OR-OptAM + SHG + 2PEF	OR-OptAM (R)	532	Hemoglobin	<0.3	4	Mouse ear morphology (*in-vivo*)	Song *et al.*, 2016
	MPM (R)	800	Collagen, NADH	<0.3	1.1	Brain morphology (*in-vivo*)	
2(3)-modes OR-OptAM + CFM + OCT* * guidance for OptAM	OR-OptAM (T)	532	Hemoglobin, Melanin	2.8	23	Mouse ear morphology (*in-vivo*)	Zhang *et al.*, 2010a; Zhang *et al.*, 2010b; Zhang *et al.*, 2011
	CFM (R)	532	Lipofuscin	2	108	Human ocular tissue morphology (*ex-vivo*)	
	OCT	830	unspecific	-	-	Rat ocular tissue morphology (*in vivo*)	
2-modes OR-OptAM + CFM	OR-OptAM (R)	570 + 593	Hemoglobin	3.9	17	Mouse ear morphology + oxygen saturation map + partial oxygen pressure	Yu Wang *et al.*, 2010; Wang *et al.*, 2011
	CFM (R)	570	unspecific	3.9	38		
2-modes OR-OptAM + CFM	OR-OptAM (T)	532	Melanin	3	23	Rabbit ocular tissue morphology (*ex-vivo*)	Tserevelakis *et al.*, 2016; Tserevelakis *et al.*, 2017; Tserevelakis *et al.*, 2020; Tserevelakis *et al.*, 2022
	CFM (R)	450	General autofluorescence	2	-	Human ocular tissue morphology (*ex-vivo*)	
						Fish scale morphology	
3-modes OR-OptAM + CFM + 2PEF	OR-OptAM (T)	570, 578	Melanin	-	-	Mouse ocular tissue morphology (*ex-vivo*)	Rao *et al.*, 2014
	CFM (R)	800	-	-	-	Plant morphology	
	MPM (R)	635	-	-	-		
2-modes AR-OptAM + SPIM	AR-OptAM (R)	420-700	Melanin, Lipids, Hemoglobin,	20-120	24	Zebrafish development (*ex-vivo*)	Lin *et al.*, 2015; Vetschera *et al.*, 2023
	SPIM (R)	420-700	GFP	2.5	36		

Table II Hybrid optoacoustic microscopy (OptAM) systems with optical coherence tomography (OCT). AR-OptAM acoustic resolution optoacoustic microscopy, OR-OptAM optical resolution optoacoustic microscopy, (T) transmission mode, (R) reflection mode, OCTA optical coherence tomography angiography, SD-OCT spectral domain optical coherence tomography, CFM confocal microscopy, FM fluorescence microscopy.

System overview	Mode	Wavelength (nm)	Contrast	Resolution lateral (µm)	Resolution axial (µm)	Applications	References
2-modes OR-OptAM + OCT	OR- OptAM (R)	800	Hemoglobin, Melanin	7	-	Rat ocular tissue morphology (*in-vivo*)	Liu *et al.*, 2015; Liu *et al.*, 2016
	OCT	800	unspecific	≈7	9.9		
2-modes OR-OptAM + SD-OCT	OR-OptAM (R)	570, 578, 588	Hemoglobin, Melanin	20	23	Rat ocular tissue morphology and retinal oxygen metabolic rate (*in-vivo*)	Song *et al.*, 2014
	SD-OCT	840	Blood flow	20	5.6		
3-modes OR-OptAM + OCT + FM	OR-OptAM (R)	532	Hemoglobin, Melanin	4.1	37	Rabbit ocular tissue morphology + assessment of retinal neovascularization	Zhang *et al.*, 2018
	OCT	905	Lipofuscin	3.8	4		
	FM	480	Fluorescein sodium	-	-		
4-modes OR-OptAM + OCT + OCT angiography (OCTA) + CFM	OR-OptAM (R)	532	Hemoglobin	6.4	31	Mouse ear morphology (*in-vivo*) + assessment of non-perfused vessels	Dadkhah *et al.*, 2019; Dadkhah and Jiao 2020
	OCT	840	unspecific	6.4	7.5		
	OCTA	840	Blood flow	-	-		
	CFM (R)	532	General autofluorescence	-	-		

(Strohm *et al.*, 2013, 2016), reaching high resolutions on the order of 1µm, using ultrasound frequencies of up to 1.2GHz. Metachromatic stained leukocytes such as single neutrophils, lymphocytes and monocytes could be identified and differentiated based on differential staining (OptAM) and US images as the biomechanical properties of the cells scatter and attenuate acoustic waves differently. A combined OCT-US-OptAM proof-of-concept setup was also reported as a 3-modality miniature probe system for the imaging of a rat ear *in-vivo*. Similarly, to other hybrid setups, OptAM visualized the vasculature system, OCT revealed the morphology of the epidermis, dermis and cartilage and US visualized anatomical features of the subcutaneous tissue.

V. ALL-OPTICAL DETECTION OF SOUND

In addition to the hybrid implementations reviewed, advances in OptA components have enabled the seamless integration of optical and OptA technology. Since its emergence in the late 1970's, OptA imaging has primarily relied on detectors developed for ultrasonography and based on piezoelectric (PZT) technology. Piezoelectric transducers are well suited for ultrasonography, since they can not only detect but also generate and guide ultrasound beams, leading to the development of medical ultrasound using cost-effective designs of one- or two-dimensional PZT transducer arrays. However, piezoelectric transducers have relatively limited bandwidths and acceptance angles (Zhang *et al.*, 2014) that capture only a part of the OptA signals generated in tissues, which results in loss of image quality. This is particularly relevant for AR-OptA microscopy and mesoscopy implementations, whereby the resolution and overall image quality and fidelity achieved depends on the frequencies captured. Moreover, the sensitivity of piezoelectric transducers, while sufficient for many macroscopic OptA applications, scales with the size of the active transducer area. Therefore, miniaturization of ultrasound detectors based on PZT technology reduces the sensitivity achieved in quadratic manner. Moreover, the size and opaqueness of PZT elements challenges the OptA illumination, imposing geometrical and delivery constraints on the imaging system designed, often leading to sub-optimal light delivery under the ultrasound detector. These challenges have led to research into alternative sound detection methods using optical techniques sensitive to vibration. This shift has given rise to OptA systems in which sound is generated and detected exclusively by optical components.

Different optical techniques are sensitive to ultrasound energy and come with different technical specifications and operational parameters. Generally, optical detection of ultrasound is based on interferometry or refractometry as exemplified in Table IV and contrasted to piezoelectric detectors.

Interferometry-based detection is based on perturbations of an interference pattern established in an optical interferometer due to mechanical changes induced by ultrasound energy, for example by generating vibrations in the resonance cavity or reflector elements. An optical detector detects these vibrations as a change of the intensity or frequency of the interferometer light to derive quantitative readings of the pressure of the impinging ultrasound wave. Several such detectors are implemented as interferometers within optical fibers, for example by embedding pi-shifted Bragg gratings (Dong *et al.*, 2017; Wissmeyer *et al.*, 2018). In this case the sensitivity does not scale with size but rather depends on the quality and sensitivity of the interferometer. Besides being transparent, optical fiber (OF) detectors attain sizes on the order of 100 micrometers in diameter and can be minimally obstructive to OptA illumination. It has been shown that it is possible to pass a side-looking fiber-based pi-shifted Bragg grating (pi-FBG) through the objective of an optical microscope (Fig.6a) and use it as the OptA detector (Shnaiderman *et al.*, 2017). This strategy allows the conversion of any optical microscope to a hybrid optical-optoacoustic microscope, without loss of optical image quality due to the optical fiber sensor. An additional advantage of this approach is that the metal casing of the optical objective can be designed to offer sound amplification by reflecting and focusing in-phase sound waves to the point in space where the OptA fiber sensor is placed. An alternative OF design is based on Fabry-Perot interferometers, which can be used for forward ultrasound detection (Fig.6b) as opposed to the side-detecting manner of pi-FBG's. In this design, detection bandwidths can increase by reducing the thickness of the resonance cavity employed (Guggenheim *et al.*, 2017) but at the expense of the sensitivity achieved (Beard *et al.*, 1999). Moreover, control of the thickness is challenging due to limitations in the required polymer deposition process (Guggenheim *et al.*, 2017). A current limitation of OF-based OptA sensors is the maximum sensing bandwidth achieved, which limits the imaging resolution to the 40µm range (Xu and Wang, 2003), as summarized in Table IV.

Several other possibilities exist for interferometry-based sound detection (Wissmeyer *et al.*, 2018), including two recent approaches, one that yielded the world's smallest ultrasound sensor and one that pushed the sensitivity limits of optical detection of ultrasound. A silicon waveguide-etalon detector (SWED) platform using 220nm thick Si waveguides demonstrated an active detection area of <0.5µm and a bandwidth of >200MHz (Fig.6c). Pressure waves perturb the optical resonator on the silicon photonics wafer and the corresponding

Table III Hybrid optoacoustic microscopy (OptAM) systems with ultrasonography (US). AR-OptAM acoustic resolution optoacoustic microscopy, OR-OptAM optical resolution optoacoustic microscopy, (T) transmission mode, (R) reflection mode, OCT optical coherence tomography.

System overview	Mode	Wavelength (nm)	Contrast	Resolution lateral (µm)	Resolution axial (µm)	Applications	References
3 modes AR-OptAM + US + Doppler US	AR- OptAM (R)	532	Hemoglobin, Melanin	140	<40	Human finger morphology (*in-vivo*) + flow detection (in phantoms only)	Harrison *et al.*, 2009; Jiang *et al.*, 2010
	US (R)	-	unspecific	180	<40		
	Doppler US (R)	-	(Liquid) flow	-	-		
2-modes AR-OptAM + US	AR-OptAM (R)	584	Hemoglobin,	130	55	Rat skull, tumor and tail morphology (*in-vivo*)	Subochev *et al.*, 2012; Subochev *et al.*, 2015
	US (R)	-	unspecific	75	30		
2-modes OR-OptAM + US	OR-OptAM (R)	532, 578	Hemoglobin	11-20	44	Mouse cranial bone and brain morphology + oxygen saturation map (*in-vivo*)	Rebling *et al.*, 2018; Estrada *et al.*, 2020
	US (R)	-	Bone	11-20	44		
2-modes AR/OR-OptAM + US	AR/OR-OptAM (R)	532	Metachromatic staining	≈1	≈1	Single cell morphology and differentiation of stained leukocytes	Strohm *et al.*, 2013; Strohm *et al.*, 2016;
	US (R)	-	unspecific	≈1	≈1		
3-modes AR/OR-OptAM + US + OCT	OR-OptAM (R)	532	Hemoglobin	13.6	42.1	Rat ear morphology (*in-vivo*)	Dai *et al.*, 2015
	US (R)	-	unspecific	>13.4	>14.3		
	OCT	1310	unspecific	13.4	14.3		

Table IV Comparison of optical, piezoelectric, and micromachined ultrasound transducers. NEP noise equivalent pressure, QPD quadrant photodiode, CCD charge-coupled device, CMOS complementary metal-oxide-semiconductor, PET polyethylene terephthalate, SU8 epoxy-based photoresist, π-BG pi-phase-shifted Bragg grating, CMUT capacitive micromachined ultrasonic transducer, PCMR plano-concave optical microresonator, N.A. not applicable, N.R. not reported (table adapted from Wissmeyer *et al.* 2018 and extended by Guggenheim *et al.* 2017; Shnaiderman *et al.* 2020; Westerveld *et al.* 2021).

Refractometric transducer	Material	Read-out element	Bandwidth (MHz)	Sensing element size (mm)	NEP (mPa/Hz$^{1/2}$)	NEP x area (mPa mm^2/Hz$^{1/2}$)	References
Intensity-sensitive	Silica	Photodiode	100	Prism (15)	100	22×10^3	Zhu *et al.*, 2017
Beam deflectometry	Coupling medium	QPD	17	Needle beam (0.09)	2.76	N.A.	Maswadi *et al.*, 2016
Phase-sensitive	Coupling medium	CCD/CMOS	110	Schlieren beam (10)	486	N.A.	Zanelli and Howard, 2006
Interferometric transducer	**Material**	**Dimensions (H × W × L, µm)**	**Q-factor**	**Conversion efficiency (M/Pa)$^{-1}$**	**NEP (mPa/Hz$^{1/2}$)**	**NEP x area (mPa mm^2/Hz$^{1/2}$)**	**References**
Micro-ring	Polystyrene	1.4 × 20 × 20 – 1.4 × 100 × 100	1.4×10^5	130×10^{-6}	5.61	1.8×10^{-3}	Maxwell *et al.*, 2008; Cheng Zhang *et al.*, 2015
	Silicon	0.5 x 15 x 15	1.1×10^4	N.R.	2.3	2.9×10^{-2}	
Fabry-Pérot	PET/Parylene C	38 × 90 × 90	2.8×10^3	90×10^{-6}	78	0.63	Zhang, Laufer, and Beard 2008; Preisser *et al.*, 2016; Rohringer *et al.*, 2016; Ashkenazi *et al.*, 2005
	SU8	10 × 15 × 15	300	N.R.	200	4.5×10^{-2}	
	Fluid with low optical absorption	$60 \times 60 \times 2 \times 10^3$	N.R.	N.R.	0.45	5.4×10^{-2}	
PCMR	PET	Ø 2.470 x 340	1.0×10^5	N.R.	1.6	7.66	Guggenheim *et al.*, 2017
π-BG	Silica	10 × 10 × 270	1.2×10^6	3.8×10^6	25	6.75×10^{-2}	Rosenthal, Razansky, and Ntziachristos 2011; Rosenthal *et al.*, 2014a; Rosenthal *et al.*, 2014b; Shnaiderman *et al.*, 2020; Westerveld *et al.*, 2021
	Silicon	0.22 x 0.5 x 26	2.2×10^4	N.R.	9	9.9×10^{-7}	
Piezoelectric transducer	**Model**	**Detector type**	**f (MHz)**	**Area (mm^2)**	**NEP (mPa/Hz$^{1/2}$)**	**NEP x area (mPa mm^2/Hz$^{1/2}$)**	**References**
Olympus NDT Panametrics	V214-BB-RM	Spherically focused piezoceramic	50	30	0.2	6	N.R.
Precision acoustics	Needle (1mm)	PVdF needle hydrophone	12	1	14.4	14.4	N.R.
Boston Scientific	Atlantis PV	Intravascular ultrasound probe	15	0.8	450	360	Wissmeyer *et al.*, 2016
Micromachined transducer	**Model**	**Detector type**	**f (MHz)**	**Area (mm^2)**	**NEP (mPa/Hz$^{1/2}$)**	**NEP x area (mPa mm^2/Hz$^{1/2}$)**	**References**
CMUT	Silicon	Array of capacitor cells	5	0.06	1.8	0.11	Khuri-Yakub and Oralkan, 2011; Wygant *et al.*, 2008

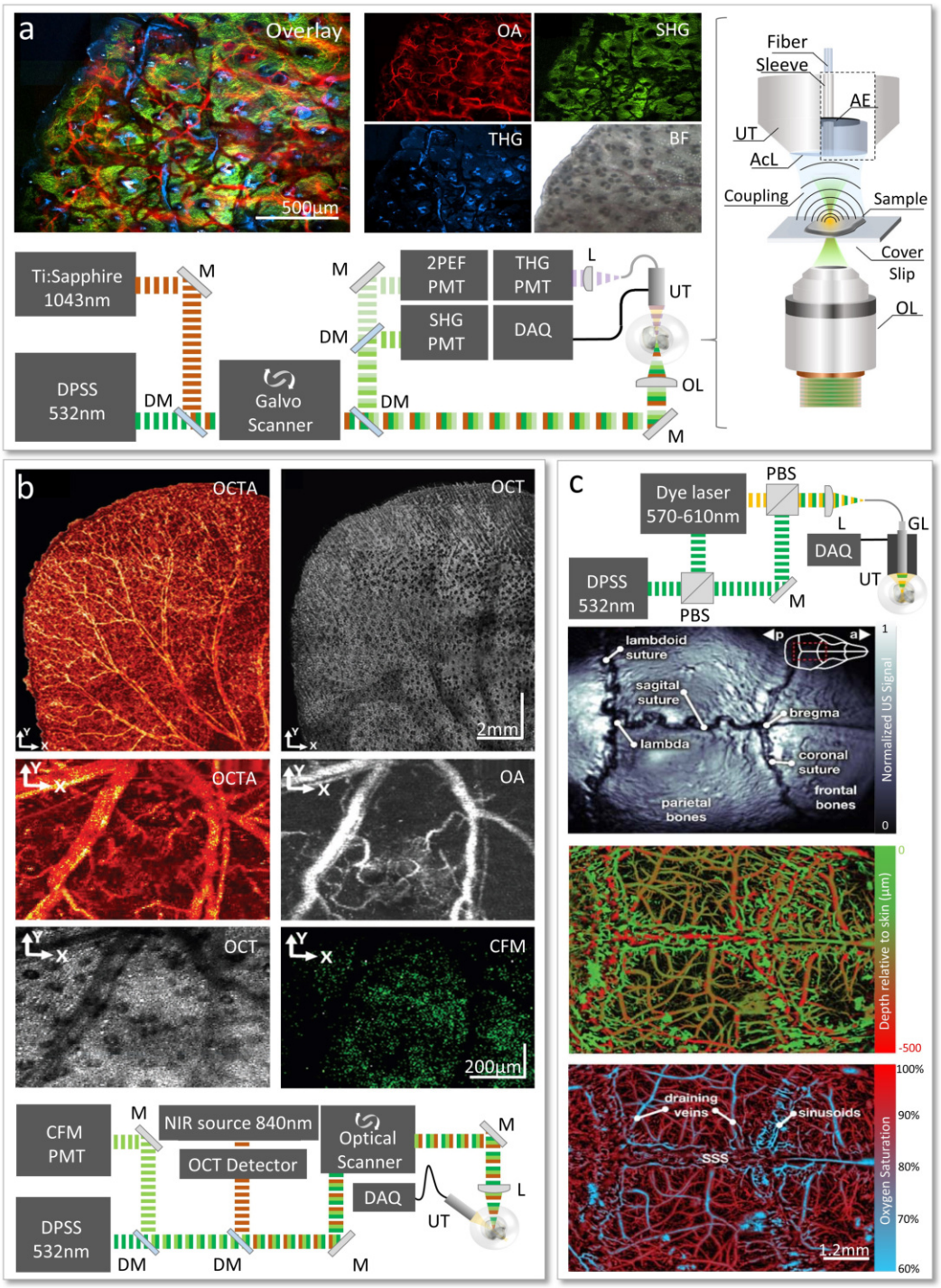

Figure 5 Hybrid optoacoustic microscopy (OptAM) schematics and applications. a) Hybrid microscopy setup involving OptAM (vasculature system), second-harmonic generation (extracellular collagen matrix), third-harmonic generation (sebaceous glands), two photon excitation fluorescence (extracellular elastin matrix) and bright-field (general tissue morphology) in the *in-vivo* imaging of a mouse ear. The schematic of the system is also included. OA optoacoustic, SHG second-harmonic generation, THG third-harmonic generation, BF bright-field, PMT photomultiplier tube, M mirror, DM dichroic mirror, OL objective lens, L lens, UT ultrasound detector, DAQ data acquisition card, AcL acoustic lens, AE active element (adapted from Seeger *et al.* 2021, 2019). b) Hybrid setup with a large-scale *in-vivo* optical coherence tomography angiography (OCTA) and optical coherence tomography (OCT) image of a mouse ear as well as small field of view images with OCTA (red, vasculature), optical-resolution-OptAM (black and white, vasculature), OCT (gray, general tissue structure) and confocal fluorescence microscopy (green, tissue autofluorescence). The schematic of the system is also included. CFM confocal fluorescence microscopy, DPSS diode pumped solid state laser, NIR near-infrared (adapted from Dadkhah and Jiao 2020). c) OptAM combined with ultrasonography (US) for structural and functional imaging of a murine cranial bone *in-vivo* with a US image (cranial bone) and two OptAM images (cranial vasculature morphology and blood oxygenation) (adapted from Rebling *et al.* 2018). PBS polarizing beamsplitter, GL GRIN lens, SSS superior sagittal sinus.

light intensity changes are recorded by a photodetector (Shnaiderman *et al.*, 2020). A second approach uses ring resonators that demonstrated sensitivities close to those of PZT elements or better. Such resonators can also be transparent to allow OptA excitation (Cheng Zhang *et al.*, 2015; Li *et al.*, 2014; Wei and Krishnaswamy, 2017). A particularly adept recently developed detector offers favorable size scalability to a fine-pitch of less than 50µm and high-sensitivity, based on a silicon photonic chip (Fig.6d). A split-rib photonic waveguide separates the rib from the slab by a small air gap and is bounded by an acoustic membrane to achieve noise-limited detection, yielding high noise-equivalent pressure sensitivity below $1.3\text{mPaHz}^{-1/2}$ for the full bandwidth (3–30MHz) and sizes that can reach 20µm. Advantageously, the split-rib waveguide can be fabricated on complementary metal-oxide-semiconductor (CMOS)-compatible technology, allowing a wide choice of membrane materials.

Detection that uses refractometry (deflectomtery) has also yielded designs that can find broad applications in OptA imaging and hybrid implementations (Manwar *et al.*, 2020; Maswadi *et al.*, 2016; Wissmeyer *et al.*, 2018). The approach uses an optical beam to interrogate the interface between two media. Ultrasound interacting with the interface induces mechanical stress that causes index of refraction changes which distort the interrogating optical beam of the interface by changing its intensity, phase or deflection angle. Then, similar to interferometry, an optical detector is employed to quantify these changes and convert them to ultrasound pressure (Wissmeyer *et al.*, 2018). Refractometry has been demonstrated in OptA measurements using position-sensitive detectors, for example a CCD camera (Nuster *et al.*, 2014) but also with conventional photodiode readouts (Hajireza *et al.*, 2017).

VI. THE TEMPORAL AND SPATIAL OPTA POINT-SPREAD-FUNCTION

In addition to implementing hybrid systems and advancing detectors better suited for OptAM, a further technical advance has shown that OptAM performance can reach that of optical systems when the impulse response of the OptA system, i.e. the OptA point-spread-function (PSF) is considered in image formation. Deconvolution using the PSF is a common operation in optical microscopy (Sibarita, 2005). However, a critical difference with the OptA method is that the OptA PSF is a delta function not only in space but also in time, the latter leading to a rich frequency spectrum. The OptA PSF depends on the geometrical characteristics of the detector employed, the bandwidth collected and the impulse response of the illumination and detection components (Deán-Ben and Razansky, 2022; Wang and Wu, 2007). An OptA system is then characterized by its TIR, which describes the system's time- and space-resolved impulse response for each point in the volume of interest (Caballero *et al.*, 2013; Seeger *et al.*, 2020).

Different approaches have been considered for obtaining the OptA impulse response and subsequently, for correcting OptA signals and images (Chowdhury *et al.*, 2020; Deán-Ben and Razansky, 2022; Lu *et al.*, 2020; Rosenthal *et al.*, 2011a; Seeger *et al.*, 2020; Strohm *et al.*, 2013; Zhang *et al.*, 2012b). A single point impulse response has been measured by focused illumination of an a ink-layer (Zhang *et al.*, 2012b). Then, Wiener-deconvolution of each scanned point achieved 1.7-fold improvement in the axial resolution compared to conventional OptA-signal processing, as demonstrated with melanoma cells *ex-vivo* and in mouse ears *in-vivo* (Zhang *et al.*, 2012b). However, the impulse response measurement at only a single point does not capture the spatial sensitivity field of the detector. Prior knowledge about the detector's geometry has been combined with scanning an OptA point source at multiple points within the sensitivity field of the detector (Chowdhury *et al.*, 2020; Lu *et al.*, 2020). This approach was demonstrated by acquiring PSF´s using a 532nm laser focused on a black carbon fiber that was 2D raster-scanned within the sensitivity field of a focused 93MHz detector (Lu *et al.*, 2020). Then, the angular spectrum approach (ASA) that models ultrasonic wave propagation (Du *et al.*, 2013; Orofino and Pedersen, 1993) was employed to model the detector geometry and reconstruct the entire TIR on a fine spatial grid yielding TIR sampling of a 0.2 x 0.2mm plane with steps of 10µm and a spatial resolution of 1.7µm. The accuracy of the ASA reconstructions was confirmed by comparing the computed results to three experimentally determined 2D-scans from three layers at different depths (Fig.7a).

In a similar approach, measurements of only a few single point OptA impulse responses together with simulations were used to synthesize the system's TIR (Chowdhury *et al.*, 2020). The electrical impulse response was extracted from the experimentally obtained OptA impulse responses and combined with simulations taking into account the detector's geometry, resulting in a synthetic TIR. Incorporating the TIR in model-based reconstruction led to an enhanced lateral and axial resolution in the center of the field of view (FOV) of 54% and 37%, respectively. Improved TIR sampling was achieved by raster-scanning a focused 50MHz detector over a 250nm thick gold layer, the latter illuminated with a focused 532nm nanosecond pulsed laser via a 2-D galvo scanner. Stepwise movement of the gold layer along the axial direction of the detector resulted in a 3D-array of time resolved OptA signals sampling the volumetric sensitivity

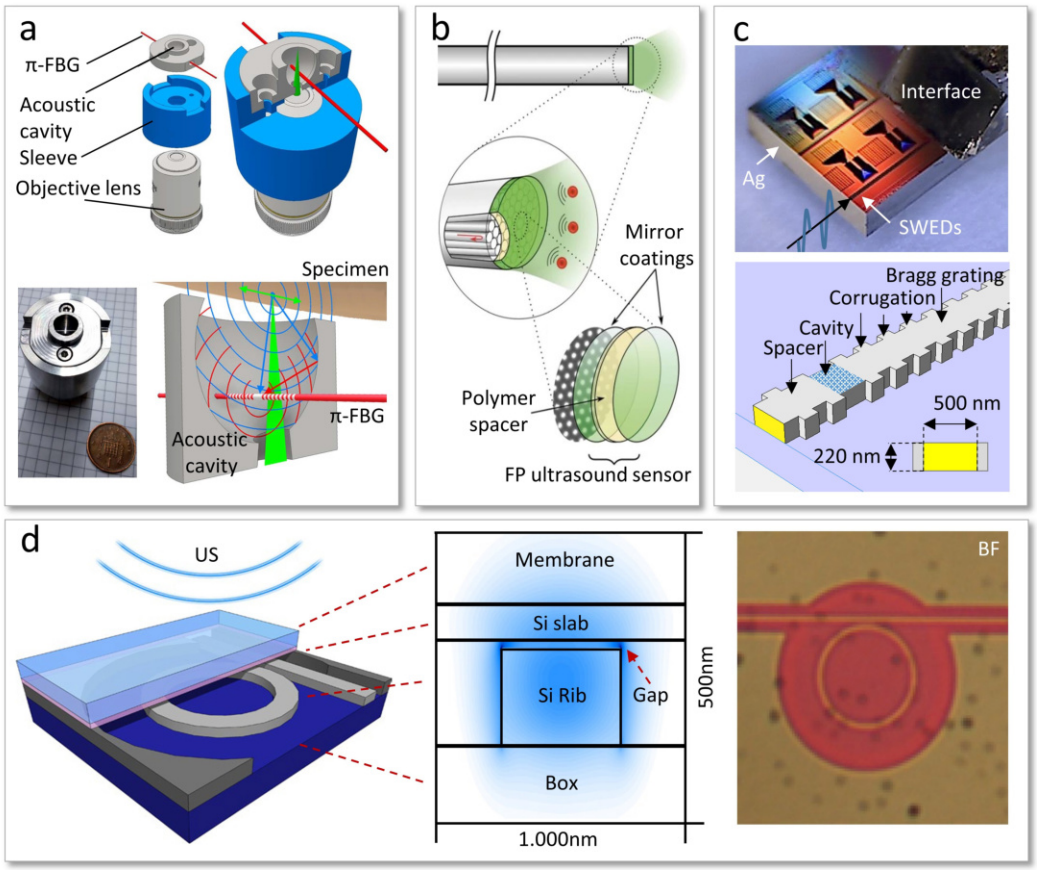

Figure 6 All-optical detection of sound. a) Side-looking fiber-based pi-shifted Bragg grating (pi-FBG) in an acoustic cavity with schematics and picture of the implementation on an objective lens (adapted from Shnaiderman *et al.* 2017). b) Structure of a Fabry-Perot (FP) interferometer-based optical fiber probe (adapted from Ansari *et al.* 2018). c) Silicon waveguide-etalon detector (SWED) photograph and schematics (adapted from Shnaiderman *et al.* 2020). d) Silicon photonic technology ring resonator schematic and optical microscope top view picture (BF) of the fabricated ultrasound sensor with semi-transparent membrane (adapted from Westerveld *et al.* 2021).

field of the detector with steps of 6.3µm and a resolution of ≈600nm (Fig.7b). Employed as a spatially matched filter, the application of the fine-grid TIR resulted in an SNR improvement of ∼5-10dB and an axial resolution improvement of 20-30% over uncorrected images, demonstrated by imaging a single red blood cell and a mouse ear *in-vivo*.

VII. LABEL-FREE DETECTION OF MOLECULAR CONTRAST

While OptA in the visible and near-infrared regimes allows the detection of only a small number of biomolecules with high sensitivity based on electronic transitions, i.e., oxy- and deoxygenated hemoglobin, lipids, water or melanin, a recent expansion of OptAM in the mid-infrared (mid-IR) significantly expands the potential to visualize different molecules without the use of contrast agents, i.e., in label-free operation. Detection in this case is based on the characteristic mid-IR spectral signatures of different molecules due to their inherent molecular vibrations, in particular bond-selective detection of specific vibrational transitions of biomolecules. Compared to conventional mid-IR spectroscopy or imaging, the OptA method operates with less attenuation due to the use of ultrasound waves for detection, and can operate in reflectance geometry due to the volumetric propagation of ultrasound waves, allowing for epi-illumination as well as trans-illumination microscopy implementations.

To capitalize on these advantages, mid-infrared optoacoustic microscopy (MiROM) was demonstrated with diffraction limited optical excitation (Pleitez *et al.*, 2020) and demonstrated absorption-contrast micrographs by raster-scanning the sample within the focal plane of the illumination, while simultaneously acquiring the OptA signal. Biomolecular specificity is achieved by tuning the emission of a tunable Quantum Cascade Laser (QCL) operating with pulses in the nanosecond range to wavelengths corresponding to specific vibrational

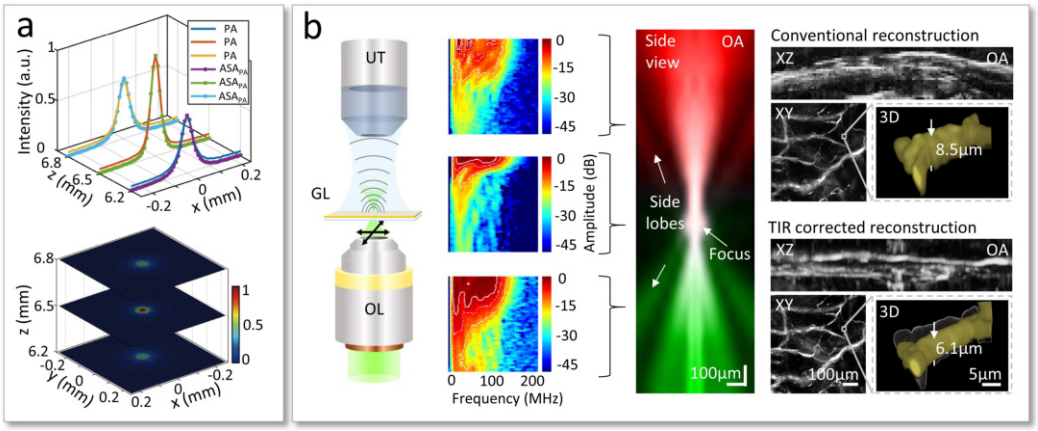

Figure 7 Point-spread-function in optoacoustic microscopy. a) Acoustic intensity distributions of a 93MHz focused ultrasound detector measured by single 2D-scans of a sub-resolution optoacoustic point source (PA) and reconstructed via the angular spectrum approach (ASA) method along the x axis and for 3 x-y-planes (adapted from Lu *et al.* 2020). b) Total impulse response (TIR) measurement with sub-resolution point sources created on a thin gold layer (GL). The frequency components of the TIR are visualized for different planes as well as the sensitivity field of the ultrasound detector (UT). TIR-corrected reconstruction led to an improved axial resolution and levelling for a mouse ear imaged with optoacoustic microscopy *in-vivo* (adapted from Seeger *et al.* 2020).

transitions. Bond-selective imaging was demonstrated by detecting lipid, protein and carbohydrate content in living HeLa cells, undifferentiated 3T3-L1/PreBAT preadipocytes and differentiated 3T3-L1 adipocytes (Fig.8a). The resolution of mid-infrared OptAM can be improved by using reading mechanisms at shorter wavelengths, e.g. in the UV (Shi *et al.*, 2019). A pulsed mid-IR laser thermally excites the sample in the focal spot. Then, a coaxially-aligned second ultraviolet laser beam optoacoustically detects the resulting transient temperature rise of the mid-IR excitation. The image is therefore created based on high resolution UV-OptAM but exhibits the specificity for vibrational contrast due to mid-IR excitation. The technique was demonstrated in fixed 3T3 mouse fibroblasts, resolving the distribution of intracellular lipids and proteins at sub-micron resolution. *Ex-vivo* label-free histological analyses of fully hydrated cerebrum and cerebellum mouse brain slices has been shown as well and resulted in OptAM images exhibiting rich structural information about the nerve fibers or fiber bundles based on myelin lipids (Fig.8b).

While the penetration depth in the mid-IR is limited by strong water absorption (Hong *et al.*, 2017; Hui *et al.*, 2016; Upputuri and Pramanik, 2019), higher penetration depth could be achieved in shortwave infrared (SWIR, 1000-2000nm) OptAM by exciting the vibrational harmonic overtones of molecules, but at the expense of lower contrast and spectral specificity due to the overlapping absorption bands (Hui et al. 2016; P. J. Harris and Altaner 2013). SWIR OptAM has been shown to resolve water and lipid content from the human skin using spectral unmixing techniques (Berezhnoi *et al.*, 2019) or collagen in a mouse tail tendon *in-vivo* (Lee *et al.*, 2018). Also, SWIR OptAM has been demonstrated in visualizing intracellular lipids in fixed human white adipocytes (Lee *et al.*, 2022)(Fig.8c).

The ability imparted by the extended OptAM spectrum is in its infancy but presents strong potential as a method to enable the visualization of functional and molecular parameters in microscopy interrogations in unperturbed cells and tissues. In the mid-IR, molecular contrast can be orders of magnitude stronger that in Raman scattering methods, owing to the strong absorption of light by different biomolecules (Pleitez *et al.*, 2020). Addition of these modes to an OptAM or hybrid system can significantly enhance the visualization abilities. Moreover, current research is geared towards utilizing specific spectral peaks to differentiate between various lipid or protein species, further enhancing the impact of this modality on molecular investigations. Operation in this extended spectral range offers a strong rationale for the use of OptA microscopy in various fields of the biomedical sciences and beyond.

VIII. REPORTER GENES

A critical next development that can further enhance the use of OptAM in biological imaging relates to recent advances in reporter genes (RG) and bacterial systems that are developed to impart strong OptA contrast (Lei *et al.*, 2020). While the invention of fluorescent proteins launched fluorescence microscopy as a definitive tool in biological research, the ability to ubiquitously generate

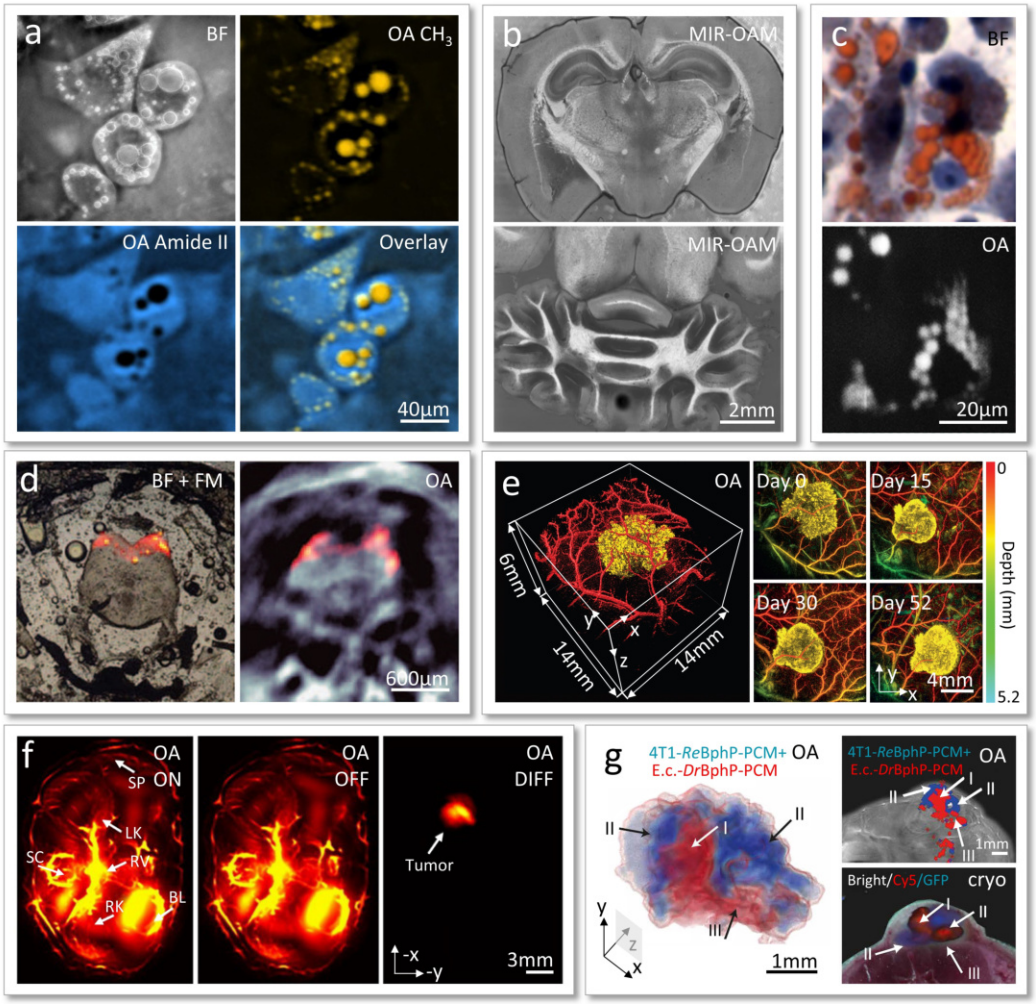

Figure 8 Extended optoacoustic contrast. a) 3T3-L1 cells imaged with bright-field (BF) and with mid-infrared optical-resolution optoacoustic microscopy (MIR OR-OptAM) at two wavelengths, revealing the CH3 and Amide II content of the cell (adapted from Pleitez *et al.* 2020). Optoacoustic (OA). b) MIR OptAM (MIR-OAM) images of myelin lipids in 300µm thick slices of the cerebrum and cerebellum (adapted from Shi *et al.* 2019). c) Fixed human white adipocytes imaged with BF (Oil-red O stain) and with shortwave infrared (SWIR) OR-OptAM revealing the CH content of the cell (adapted from Lee *et al.* 2022). d) Fluorescent histology and optoacoustic tomography image of the hindbrain area of a six-month-old zebrafish with mCherry expression shown in orange/red (adapted from Razansky *et al.* 2009). e) Tyr expressing K562 cells after subcutaneous injection into the flank of a nude mouse and longitudinal progression over 52 days (adapted from Jathoul *et al.* 2015). Fluorescence microscopy (FM). f) *In-vivo* whole-body OptA tomography images of the kidney region of a nude mouse with the ON-OFF state images visualizing the major blood-enriched internal organs and the differential image (DIFF) clearly indicating a tumor. Right kidney (RK), spinal cord (SC), renal vein (RV), bladder (BL), spleen (SP) (adapted from Yao *et al.* 2016). g) *In-vivo* OptA imaging (3D representation left and 2D image upper right) of a 4T1 tumor stably expressing the photo-switchable protein ReBphP-PCM (arrows II and III) immediately after injecting *E. coli* expressing the photo-switchable protein DrBphP-PCM (arrow I). Histology confirmation (lower left) is inferred from fluorescence in DrBphP-PCM (Cy5 only) and ReBphP-PCM (GFP primarily) (adapted from Mishra *et al.* 2020).

specific and strong contrast from cells and subcellular components has been lacking in OptA methods. Early attempts to use lacZ encoding b-galactosidase (Li *et al.*, 2006, 2007) or tyrosinase for the production of melanin (Jathoul *et al.*, 2015; Stritzker *et al.*, 2013), did not result in methodology with high dissemination potential. While b-galactosidase and melanin are strong light absorbers that are well suited for strong OptA signal generation, they come with limitations for biomedical use. b-galactosidase absorbs in the deep blue and UV that limits the contrast due to strong background absorption and the penetration of OptA methods. Melanin has a flat spectrum that also competes with strong background contrast from hemoglobin for *in-vivo* applications and its expression may be toxic to many cells. Nevertheless, a tyrosinase-based genetic reporter

worked well with visualizing vaccinia virus-mediated melanin production in mouse models, demonstrating a powerful approach to visualize oncolytic approaches in high-resolution (Stritzker *et al.*, 2013). The same reporter was also employed to visualize tyrosinase expressing human lymphoblast (K562) xenografts in mice *in-vivo* over 52 days (Fig7.e) (Jathoul *et al.*, 2015). However, our attempts to express the virus ubiquitously in cells generally resulted in poor survival, possibly contributing to the lack of widespread adoption of this reporter system in OptA studies.

Fluorescent proteins (FP) have also been considered as OptA reporters (Lei *et al.*, 2020). Enhanced green fluorescent protein (eGFP) and mCherry have been imaged in *Drosophila melanogaster* pupa and adult zebrafish *in-vivo* using a multispectral OptA tomography setup (Razansky *et al.*, 2009). Spectral unmixing was employed to improve the specificity in visualizing salivary glands modified to specifically express eGFP in intact pupa. Likewise, the hindbrain area expressing mCherry was visualized in high-resolution in a six-month old zebrafish, despite the highly scattering conditions (Fig.8d). However, the challenge with FPs is that they are optimized to convert the energy absorbed into fluorescence re-emission, and may offer low absorption cross-sections. These factors reduce the contrast available for OptA signal generation. Therefore, the sensitivity of OptA methods when using FPs does not match that of fluorescence microscopy. Moreover, when it comes to intravital imaging, fluorescence detection generally operates on low background tissue auto-fluorescence, maximizing contrast, compared to OptA FP detection which competes with the absorption of other background chromophoric molecules such as hemoglobin. Spectral unmixing approaches can be enlisted to differentiate photo-absorbing molecules over background chromophores based on their spectral characteristics. Another approach that improves intravital contrast is operation with labels that exhibit absorption peaks in the near-infrared (NIR), a spectral region where light absorption by tissue is significantly lower than in the visible or mid-IR, as demonstrated on mouse xenografts using breast cancer cells expressing two near-infrared fluorescent proteins iRFP670 and iRFP720 (Krumholz *et al.*, 2014). The use of non-fluorescent chromo-proteins that do not exhibit radiative relaxation has also been considered to improve upon the limitations of fluorescent proteins. For example, *E. coli* expressing the chromoprotein Ultramarine were injected in the ear of an anaesthetized rat and imaged at multiple wavelengths with subsequent spectral unmixing for hemoglobin and the chromoproteins, using an AR-OptAM system (Li *et al.*, 2016). Significant progress was also made using violacein, which leads to strong OptA contrast (Weber *et al.*, 2016). Violacein is another naturally occurring and photobleaching-resistant deep purple chromophore originally found in the *Chromobacterium violaceum* bacterium and enzymatically generated from the sole precursor tryptophan. *E. coli* bacteria expressing essential enzymes for the synthesis of violacein were grown and imaged with an OR-OptAM system (Jiang *et al.*, 2015), demonstrating the *in-vivo* imaging possibility of this reporter system as well.

Recently, a new concept has emerged that promises to impart high-molecular sensitivity and specificity by differentiating contrast in the time domain. In particular, recent advances in the use of photo-switchable labels, developed and adapted to OptA requirements (Mishra *et al.*, 2019; Stiel *et al.*, 2015; Yao *et al.*, 2016) enable detection of OptA contrast that is modulated by an external energy source, such as light. Using lock-in detection or similar techniques that can detect the modulation pattern or differences in the signal imposed because of it, contrast is generated only from labelled moieties. This principle has been demonstrated with fluorescent proteins (Dronpa) for the discrimination of protein filled tubes in the presence of highly-absorbing blood (Stiel *et al.*, 2015). A photo-switchable bacterial phytochrome (BphP1) with spectral properties defined by biliverdin IXα was shown to enhance the OR-OptAM contrast of glioblastoma cancer cells (Yao *et al.*, 2016) or of T lymphocytes and bacteria (Mishra *et al.*, 2020) implanted in mouse organs such as kidneys (see Fig.8f) and brains or body (see Fig.8g). Recently, a genetically encoded photo-switchable Ca^{2+} sensor rsGCaMP1 based on GCaMP, a genetically encoded calcium indicator, has been conceptually demonstrated in implanted cells in mice *in-vivo* with an OptA tomography setup (Mishra *et al.*, 2022). HeLa cells expressing rsGCaMP1 were subcutaneously implanted into the back of a mouse and imaged with OptA. The signals could clearly be delineated based on photo-switching and were used to differentiate between relative Ca^{2+} concentrations.

Photo-switching may yield a ubiquitous approach for biological imaging using OptAM, since it offers the potential for significantly higher background suppression over spectral techniques, especially in *in-vivo* imaging. In this role it may play an essential role in OptAM, serving as the fluorescent protein analogue to the OptA method. We anticipate that progress with labels and hardware that enables sensitive implementation of photo-switching concepts will generate additional modes of operation in hybrid OptAM systems and enable visualization of elaborate biological contrasts deeper than what is possible with optical microscopy.

IX. MULTIMODAL AND MULTI-CONTRAST OPERATION

The combination of advances in hybrid systems, optical methods for ultrasound detection and TIR correction with new molecular contrast techniques facilitates the implementation of multiple imaging modes and ability to resolve a large number of morphological, functional and cellular or molecular parameters, going well beyond the early OptA demonstrations in imaging microvasculature. Therefore, a hybrid optical-optoacoustic system could advance from a few modes of visualization, for example 6 modes as discussed in Section IV, to visualizing a large number of biological parameters. This can be achieved by capitalizing on the extended spectrum possibilities when visualizing absorption contrast as well as when using spectral techniques and the possibility of adding temporal unmixing of photo-switchable OptA labels.

An example of multi-contrast generation was recently based on the use of a super-continuum source providing white-light nanosecond pulses with a spectral range from 475-2400nm (Nteroli *et al.*, 2022), as part of a hybrid OR-OptAM and OCT system. The spectrally wide pulses from the super-continuum laser were narrowed down to the wavelength of interest by bandpass filters with 25nm and 50nm linewidths in the range between 475 to 1650nm and guided into the hybrid system. A second supercontinuum source was employed as the source for the OCT channel. The system was demonstrated *in-vivo* in a multimodal approach by showing the anatomy of a tadpole (Fig.9a) with OCT and overlaying the anatomical images with linearly unmixed OR-OptAM images of melanin and hemoglobin (VIS OR-OptAM) as well as collagen, glucose and lipids (NIR/SWIR OR-OptAM). This example showcases how the OptA modality can capitalize on spectra to resolve, in this case, 5 sources of contrast (5 molecules). The addition of mid-IR illumination could reveal several more molecules, including different lipids and proteins. Therefore, label-free OptAM operation over the visible and infrared could resolve at least 10 tissue molecules. By adding OptA temporal unmixing, hybrid fluorescence microscopy and other modes such as second and third-harmonics, it is possible to deliver microscopes that could visualize 20 or more molecules and their corresponding functions and structures, building more complete pictures of the observed target.

Another unique mode of operation is the combination of OR- and AR modes. As discussed in Section IV, it is possible to utilize one ultrasound detector with focused and broad illumination and enable multi-scale OptA interrogation at optical diffraction and acoustic diffraction resolutions reaching deeper than conventional optical microscopy. Such operation can be employed to visualize deeper into tissue samples or into large organisms (see Section IV.A), but also to improve imaging navigation by allowing the visualization of large fields of view using AR-OptAM and zoom-in operations at higher resolution using OR-OptAM and hybrid optical microscopy (Fig.9b). An alternative method for generating concurrent OR and AR-OptAM was demonstrated using co-axial focused illumination through a gradient-index (GRIN) lens and ultrasound detection using a spherically-focused ultrasound element (Fig.9c) (Estrada *et al.*, 2014). The design and placement of the GRIN lens allows a user to adjust the location of the two foci with respect to the sample surface to enable OptAM with optical resolution at superficial depths that blends into acoustic-resolution for deeper tissue layers. The system has been demonstrated in transcranial imaging of the brain of a nude mouse *in-vivo* after removing the scalp (Fig.9c). Imaging of a 4x5mm FOV revealed the brain cortical vasculature on a large scale while zooming in allowed the identification of smaller capillaries in the range of the resolution of the OR-OptAM mode.

X. DISCUSSION, CHALLENGES & OUTLOOK

The fundamental advantages of the OptA method relate to offering high-resolution optical interrogation of light absorption by molecules and enabling visualization deeper than optical microscopy (Ntziachristos, 2010). However, despite technical advances and demonstrations in pilot studies, OptAM has not yet impacted biomedical sciences in a broad sense. A key reason is that the new ability must be coupled to contrast and sensitivity that addresses unmet need in biological investigations.

Initial demonstrations of OptAM focused on imaging microvasculature due to the strong contrast offered by concentrated hemoglobin in the vascular system. Being a strong absorber in the visible region, hemoglobin offered a convenient test bed to demonstrate system capabilities. Microvasculature and microvascular oxygenation is an important patho-physiological target with implications in many disease conditions (Beard, 2011; Karlas *et al.*, 2021; Wang and Hu, 2012) and in biological observation (Taboada *et al.*, 2022). However, biological imaging has much broader demands, requiring visualization of a multitude of cellular and molecular functions. Given the powerful observations already offered by optical microscopy techniques, OptA imaging may find critical applications in visualizing at greater depths and offering additional biological information through novel contrast mechanisms, especially when considered in hybrid implementations with established methods. The hybrid optical and OptA systems reviewed point toward that direction as they offer an innovative combination of

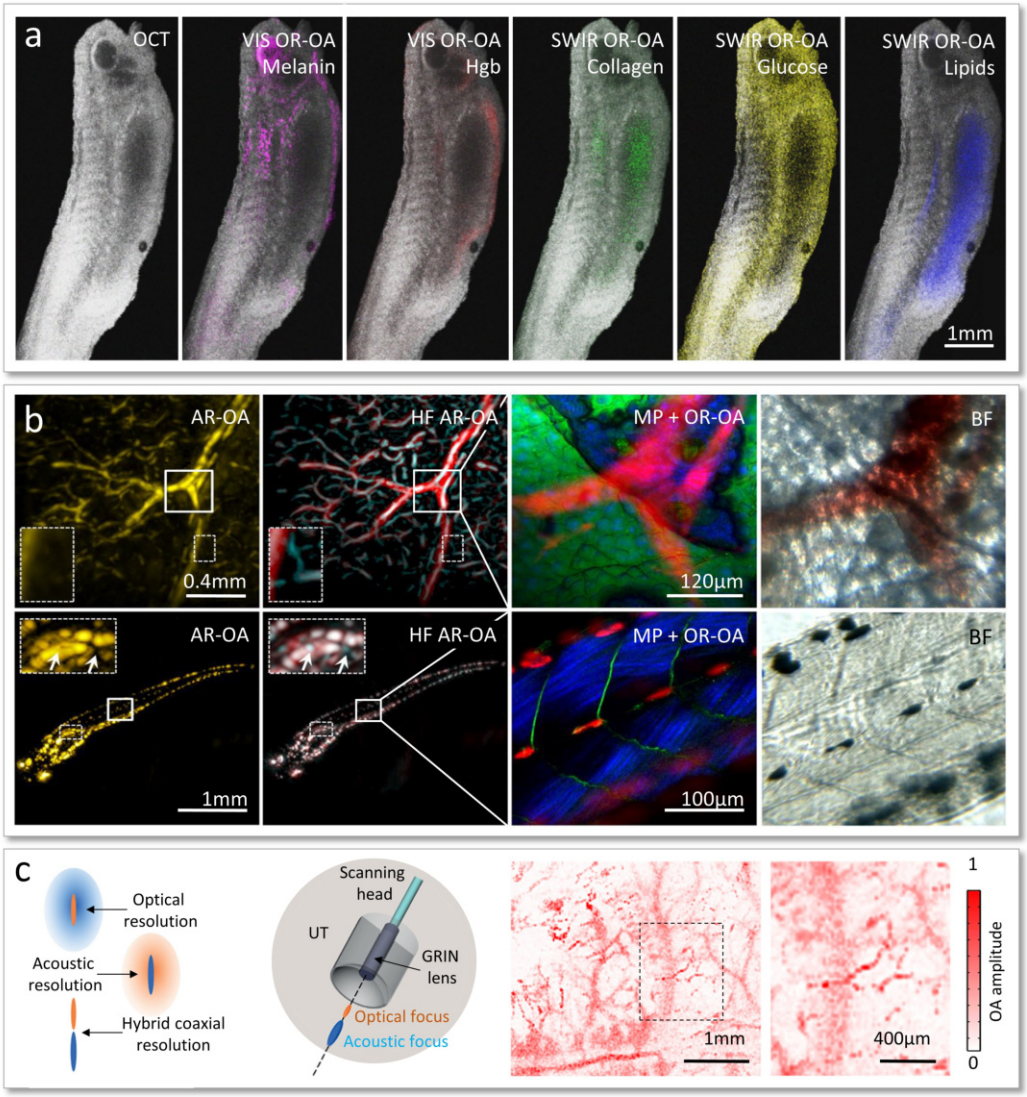

Figure 9 Multimodal operation in optoacoustic microscopy (OptAM): a) Qualitative illustrations of the superposition of a tadpole's optical coherence tomopgrahy (OCT) image with visible light optical-resolution OptAM (VIS OR-OptAM) revealing the melanin (pink) and hemoglobin content (magenta) and shortwave infrared (SWIR) OR-OptAM revealing collagen (green), glucose (yellow) and lipids (blue). Adapted from Nteroli *et al.* 2022. Optoacoustic (OA). b) 6-modal multi-scale, multi-contrast visualization of a mouse ear (upper row) and zebrafish larva (lower row) with acoustic-resolution Opt-AM (AR-OptAM) while high frequency (HF) AR-OptAM visualizes high frequency components in turquoise for the coarse structure of the specimen and zoomed in areas with OR-OptAM, multiphoton (MP) and bright-field (BF). AR- and OR-OptAM contrast is generated from hemoglobin in the mouse ear and from melanocytes in the zebrafish larva (visualized in red in the zoomed in area). Second-harmonic generation (SHG) contrast is generated from dermal collagen in the mouse ear and collagen of the fish musculature for the zebrafish larva (visualized in blue). Third-harmonic generation (THG) contrast is generated from keratinocytes in the hair follicles and dermis for the mouse ear and connective tissue for the zebrafish larva (visualized in green). Adapted from Soliman *et al.* 2016. c) Combined OR-AR setup with separate illumination demonstrated in the imaging of the brain vasculature at a higher and lower scale *in-vivo*. GRIN gradient-index. UT ultrasound detector. Adapted from Estrada *et al.* 2014.

contrast and/or depth that is not available in any of the modalities alone. Likewise, in addition to the impressive technical developments in Sections IV-VI, a particularly promising advance is the generation of multimodal contrast that utilizes extended spectra (Section VII) or novel biotechnology approaches (Section VIII) to visualize contrast that covers a broader spectrum of biological interrogations and complements the elaborate interrogations already allowed by optical microscopy.

Expanding the contrast available to microscopy is a critical development and one of the great challenges of biological imaging in general and intravital microscopy in particular. Biomedical research is in need of capturing

complex interactions between several different systems on the tissue, cellular and molecular levels. In particular, functional interrogations require *in-vivo* studies, i.e., an area of investigation whereby optical tissue sectioning techniques become necessary. Therefore, as OptAM developments transform from technology validation studies to advancing biomedical knowledge or developing solutions for medicine and healthcare, the use of multi-modal and multi-contrast abilities becomes particularly critical. In this vein, hybrid implementations with OptAM are a promising approach for expanding the contrast available to intravital optical microscopy. The CFM, 2PEF/3PEF and FM modes of the systems in Section IV mainly rely on fluorescence and can resolve NADH, lipofuscin, elastin and fluorescent proteins or other fluorescent reporters. Other modes or modalities, such as second and third-harmonic generation, OCT or ultrasound can resolve structural tissue elements such as collagen, lipids and tissue interfaces. Then, as discussed in Section IX, the addition of OptAM to resolve absorption offers a fundamentally different direction of contrast generation through label-free imaging of absorption and reporters based on absorption rather than fluorescence.

Using optical detection, as discussed in Section V, it is possible to seamlessly integrate OptAM contrast into optical microscopes. Coming with broadband performance, optical detection also allows scalable resolution and penetration depth, possibly reaching resolutions in the sub-10 micrometer scale or better, matching more closely the operation of optical microscopes even in AR mode. This is a promising feature of the OptA method as it could be employed as an add-on to optical microscopy, even in the currently installed base of systems. Coupled with accurate TIR characterization, as discussed in Section VI, optical detection of sound can be also utilized for high-fidelity imaging, enabling both OR and AR modes.

Another interesting direction of OptAM relates to label-free detection of molecules, as per Section VII. Similar to Raman methods, label-free OptA molecular sensing opens possibilities for the study of unperturbed systems and monitoring of specific molecular species. Using mid-IR absorption, OptA detection is up to 3 orders of magnitude more sensitive than Raman spectroscopy (Pleitez *et al.*, 2020), although the performance in particular applications should be contrasted to signal enhancing Raman methods such as coherent anti-Stokes Raman scattering (CARS) or stimulated Raman scattering (SRS). For example a recent development demonstrates how OptAM can detect glucose with high accuracy (Uluç *et al.*, 2024), possibly with higher sensitivity that Raman detection. The major limitation of mid-IR OptA is that it only reaches depths of ∼140 micrometers (Uluç *et al.*, 2024) due to the high absorption of light by water/tissue in the mid-IR. Nevertheless, mid-IR OptAM offers non-invasive operation, in contrast to electrochemical sensors or other technologies, so that it can also be applied to unperturbed environments. The approach can also be employed for label-free characterization of excised tissue (Visscher *et al.*, 2022), a mode that could become useful in stand-alone OptAM systems, not only hybrid implementations. Another area of investigation relates to shifting towards shorter excitation wavelengths with X-ray OptA (Xiang *et al.*, 2016) or ionoacoustics (Kellnberger *et al.*, 2016). However, the use of ionizing radiation and relatively low absorption of high energies by tissue may limit biological applications.

Going beyond biomedical microscopy, stand-alone OptA imaging can be useful in clinical translation and human applications, as underscored by the emergence of several companies commercializing OptA systems such as iThera Medical (Germany), OPTICHO (South Korea), Kyodo (Japan), Luxonus (Japan), FUJIFILM, VisualSonics (Canada), Seno Medical (USA) and Photosound (USA). These systems are broadly utilized in human and animal studies based primarily on hemoglobin signals or for research with OptA agents and nanoparticles. They operate with frequencies in the few MHz (macroscopy) to a few tens of MHz (mesoscopy), rendering resolutions in the few hundreds to a few tens of micrometers respectively (Omar, Aguirre, and Ntziachristos 2019). Microvasculature and blood oxygenation patterns have been shown to resolve angiogenesis, hypoxia or inflammatory signals associated with cancer, inflammatory skin diseases and several other indications (Aguirre *et al.*, 2017; Favazza *et al.*, 2011; He *et al.*, 2022; Lin *et al.*, 2021; Nau *et al.*, 2023; Omar *et al.*, 2019; Oraevsky *et al.*, 2018; Zhang *et al.*, 2009). Macroscopic implementations have also been explored in imaging cancer, cardiometabolic parameters, lipid dynamics and other conditions (Karlas *et al.*, 2021; Li *et al.*, 2018; Reber *et al.*, 2018) or response to pharmaceuticals (Taboada *et al.*, 2022).

The extent by which OptAM and imaging will become as common to biomedical interrogations as mainstream optical microscopy approaches will depend on the particular applications that will be enabled by the technological and especially the contrast generation advances. Broad adoption of the new modality may be particularly compelling in research areas relating to organ on a chip and tissue engineering (Feinberg *et al.*, 2007; Haraguchi *et al.*, 2012; Huh *et al.*, 2010; Lancaster *et al.*, 2013; Ronaldson-Bouchard *et al.*, 2022; Sato and Clevers, 2013). Development of tissues and (mini-)organs in the laboratory requires observation and control at multiple levels of tissue organization and function. Therefore, the functional imaging abilities and depth penetration imparted

by OptA, including label-free molecular sensing and the superb ability for imaging microvasculature and oxygen exchange may be critical for a detailed understanding of processes driving tissue viability and function. Similarly, we expect OptA methods to solidify their utility in intravital applications in animal and human research and potentially offer healthcare solutions in diagnostics and theranostics based on the microvasculature and metabolic readings. On the other hand, implementations that exchange depth for resolution, resembling optical microscopy in performance, are probably best implemented with optical microscopes in a hybrid fashion to combine the established utility of optical methods with the new features offered by optoacoustics. Developments in imparting cellular and sub-cellular contrast, for example using photo-switching techniques, may truly render a highly compelling biological imaging modality that could offer visualization beyond the limits of optical microscopy, yielding, in the future, to standalone OptAM systems with high dissemination potential.

XI. ACKNOWLEDGMENTS

This work was supported by the Deutsche Forschungsgemeinschaft (DFG) as part of the CRC 1123 (Z1). The authors also thank Dr. Elisa Bonnin and Dr. Serene Lee for their attentive reading and improvements of the manuscript.

REFERENCES

Aguirre, J, B. Hindelang, Andrei Berezhnoi, U. Darsow, F. Lauffer, K. Eyerich, T. Biedermann, and V. Ntziachristos (2018), "Assessing nailfold microvascular structure with ultra-wideband raster-scan optoacoustic mesoscopy," Photoacoustics **10**, 31–37.

Aguirre, Juan, Mathias Schwarz, Natalie Garzorz, Murad Omar, Andreas Buehler, Kilian Eyerich, and Vasilis Ntziachristos (2017), "Precision assessment of label-free psoriasis biomarkers with ultra-broadband optoacoustic mesoscopy," Nature Biomedical Engineering **1** (5), 0068.

Andreev, Valeri G, Dmitriy A. Popov, Dmitriy V. Sushko, Alexander A. Karabutov, and Alexander A. Oraevsky (2002), "Image reconstruction in 3D optoacoustic tomography system with hemispherical transducer array," (San Jose, CA) pp. 137–145.

Ansari, Rehman, Edward Z. Zhang, Adrien E. Desjardins, and Paul C. Beard (2018), "All-optical forward-viewing photoacoustic probe for high-resolution 3D endoscopy," Light: Science and Applications **7** (1), 10.1038/s41377-018-0070-5, number: 1 Publisher: Springer US.

Asao, Yasufumi, Yohei Hashizume, Takahiro Suita, Ken-ichi Nagae, Kazuhiko Fukutani, Yoshiaki Sudo, Toshikazu Matsushita, Shuichi Kobayashi, Mariko Tokiwa, Iku Yamaga, Elham Fakhrejahani, Masae Torii, Masahiro Kawashima, Masahiro Takada, Shotaro Kanao, Masako Kataoka, Tsuyoshi Shiina, and Masakazu Toi (2016), "Photoacoustic mammography capable of simultaneously acquiring photoacoustic and ultrasound images," Journal of Biomedical Optics **21** (11), 116009.

Ashkenazi, Shai, Yang Hou, Takashi Buma, and Matthew O'Donnell (2005), "Optoacoustic imaging using thin polymer étalon," Applied Physics Letters **86** (13), 134102.

Aumann, Silke, Sabine Donner, Jörg Fischer, and Frank Müller (2019), "Optical Coherence Tomography (OCT): Principle and Technical Realization," in *High Resolution Imaging in Microscopy and Ophthalmology*, edited by Josef F. Bille (Springer International Publishing, Cham) pp. 59–85.

Bailey, Brent, Daniel L. Farkas, D. Lansing Taylor, and Frederick Lanni (1993), "Enhancement of axial resolution in fluorescence microscopy by standing-wave excitation," Nature **366** (6450), 44–48, number: 6450.

Beard, Paul (2011), "Biomedical photoacoustic imaging," Interface Focus **1** (4), 602–631, number: 4.

Beard, PC, F. Perennes, and T.N. Mills (1999), "Transduction mechanisms of the Fabry-Perot polymer film sensing concept for wideband ultrasound detection," IEEE Transactions on Ultrasonics, Ferroelectrics and Frequency Control **46** (6), 1575–1582.

Bell, Kevan, Lyazzat Mukhangaliyeva, Layla Khalili, and Parsin Haji Reza (2021), "Hyperspectral absorption microscopy using photoacoustic remote sensing," Optics Express **29** (15), 24338, number: 15.

Berezhnoi, Andrei, Juan Aguirre, Benedikt Hindelang, Natalie Garzorz-Stark, Murad Omar, Ulf Darsow, Kilian Eyerich, and Vasilis Ntziachristos (2019), "Optical features of human skin revealed by optoacoustic mesoscopy in the visible and short-wave infrared regions," Optics Letters **44** (17), 4119.

Bondu, M, M. J. Marques, P. M. Moselund, G. Lall, A. Bradu, and A. Podoleanu (2018), "Multispectral photoacoustic microscopy and optical coherence tomography using a single supercontinuum source," Photoacoustics **9**, 21–30, publisher: Elsevier GmbH.

Caballero, M A A, A. Rosenthal, A. Buehler, D. Razansky, and V. Ntziachristos (2013), "Optoacoustic determination of spatio- temporal responses of ultrasound sensors," IEEE Transactions on Ultrasonics, Ferroelectrics, and Frequency Control **60** (6), 1234–1244.

Callisen, F I (1947), "An Optical-Acoustic Method of Gas Analysis," Nature **159** (4031), 167–167, number: 4031.

Carome, E F, N. A. Clark, and C. E. Moeller (1964), "Generation of Acoustic Signals in Liquids by Ruby Laser-Induced Thermal Stress Transients," Applied Physics Letters **4** (6), 95–97, number: 6.

Chalfie, Martin, Yuan Tu, Ghia Euskirchen, William W. Ward, and Douglas C. Prasher (1994), "Green Fluorescent Protein as a Marker for Gene Expression," Science **263** (5148), 802–805, number: 5148.

Chen, QX, R.J. Dewhurst, P.A. Payne, and A. Davies (1993), "Photo-acoustic probe for intra-arterial imaging and therapy," Electronics Letters **29** (18), 1632.

Cheng Zhang,, Sung-Liang Chen, Tao Ling, and L. Jay Guo (2015), "Review of Imprinted Polymer Microrings as Ultrasound Detectors: Design, Fabrication, and Characterization," IEEE Sensors Journal **15** (6), 3241–3248.

Chowdhury, Kaushik Basak, Jaya Prakash, Angelos Karlas, Dominik Justel, and Vasilis Ntziachristos (2020), "A Synthetic Total Impulse Response Characterization Method for Correction of Hand-Held Optoacoustic Images," IEEE Transactions on Medical Imaging **39** (10), 3218–3230, num-

ber: 10.
Cox, B T, S. Kara, S. R. Arridge, and P. C. Beard (2007), "k -space propagation models for acoustically heterogeneous media: Application to biomedical photoacoustics," The Journal of the Acoustical Society of America **121** (6), 3453–3464.
Dadkhah, Arash, and Shuliang Jiao (2020), "Integrating photoacoustic microscopy, optical coherence tomography, OCT angiography, and fluorescence microscopy for multimodal imaging," Experimental Biology and Medicine **245** (4), 342–347, number: 4.
Dadkhah, Arash, Jun Zhou, Nusrat Yeasmin, and Shuliang Jiao (2019), "Integrated multimodal photoacoustic microscopy with OCT- guided dynamic focusing," Biomedical Optics Express **10** (1), 137, number: 1.
Dai, Xianjin, Lei Xi, Can Duan, Hao Yang, Huikai Xie, and Huabei Jiang (2015), "Miniature probe integrating optical-resolution photoacoustic microscopy, optical coherence tomography, and ultrasound imaging: proof-of-concept," Optics Letters **40** (12), 2921, number: 12.
Davidovits, Paul, and M. David Egger (1969), "Scanning Laser Microscope," Nature **223** (5208), 831–831.
Deihl, David T, and F. Roy Carlson (1968), ""N Waves" from Bursting Balloons," American Journal of Physics **36** (5), 441–444, number: 5.
Delany, Michael Edward (1959), "The optic-acoustic effect in gases," Science Progress (1933-) **47** (187), 459–467, publisher: JSTOR.
Denk, Winifried, James H. Strickler, and Watt W. Webb (1990), "Two-Photon Laser Scanning Fluorescence Microscopy," Science **248** (4951), 73–76.
Deán-Ben, X Luís, Daniel Razansky, and Vasilis Ntziachristos (2011), "The effects of acoustic attenuation in optoacoustic signals," Physics in Medicine and Biology **56** (18), 6129–6148.
Deán-Ben, Xosé Luís, and Daniel Razansky (2022), "A practical guide for model-based reconstruction in optoacoustic imaging," Frontiers in Physics **10**, 1028258.
Diebold, G J, M. I. Khan, and S. M. Park (1990), "Photoacoustic "Signatures" of Particulate Matter: Optical Production of Acoustic Monopole Radiation," Science **250** (4977), 101–104.
Diebold, G J, T. Sun, and M. I. Khan (1991), "Photoacoustic monopole radiation in one, two, and three dimensions," Physical Review Letters **67** (24), 3384–3387.
Diot, Gael, Stephan Metz, Aurelia Noske, Evangelos Liapis, Barbara Schroeder, Saak V. Ovsepian, Reinhard Meier, Ernst Rummeny, and Vasilis Ntziachristos (2017), "Multispectral Optoacoustic Tomography (MSOT) of Human Breast Cancer," Clinical Cancer Research **23** (22), 6912–6922, number: 22.
Dogan, Basak E, Gisela L. G. Menezes, Reni S. Butler, Erin I. Neuschler, Roger Aitchison, Philip T. Lavin, F. Lee Tucker, Stephen R. Grobmyer, Pamela M. Otto, and A. Thomas Stavros (2019), "Optoacoustic Imaging and Gray-Scale US Features of Breast Cancers: Correlation with Molecular Subtypes," Radiology **292** (3), 564–572.
Dong, Biqin, Cheng Sun, and Hao F. Zhang (2017), "Optical Detection of Ultrasound in Photoacoustic Imaging," IEEE Transactions on Biomedical Engineering **64** (1), 4–15.
Du, Yigang, Henrik Jensen, and Jørgen Arendt Jensen (2013), "Investigation of an angular spectrum approach for pulsed ultrasound fields," Ultrasonics **53** (6), 1185–1191, number: 6.
Duck, Francis (1990), *Physical properties of tissue: a comprehensive reference book* (Institute of Physics and Engineering in Medicine, York).
Englert, Ludwig, Maria Lacalle-Aurioles, Nguyen-Vi Mohamed, Paula Lépine, Mathur Meghna, Vasilis Ntziachristos, Thomas M Durcan, and Juan Aguirre (2023), "Fast 3D Optoacoustic Mesoscopy of Neuromelanin Through Entire Human Midbrain Organoids at Single-Cell Resolution," Laser Photonics Rev https://doi.org/10.1002/lpor.202300443.
Estrada, Héctor, Johannes Rebling, Urs Hofmann, and Daniel Razansky (2020), "Discerning calvarian microvascular networks by combined optoacoustic ultrasound microscopy," Photoacoustics **19**, 100178.
Estrada, Héctor, Jake Turner, Moritz Kneipp, and Daniel Razansky (2014), "Real-time optoacoustic brain microscopy with hybrid optical and acoustic resolution," Laser Physics Letters **11** (4), 045601.
F. J. W. W, (1911), "The Dynamical Theory of Sound. By Horace LambF. R. S. , 1910. (Edward Arnold)," The Mathematical Gazette **6** (94), 161–162.
Favazza, Christopher P, Lihong V. Wang, Omar W. Jassim, and Lynn A. Cornelius (2011), "In vivo photoacoustic microscopy of human cutaneous microvasculature and a nevus," Journal of Biomedical Optics **16** (1), 1, number: 1.
Feinberg, Adam W, Alex Feigel, Sergey S. Shevkoplyas, Sean Sheehy, George M. Whitesides, and Kevin Kit Parker (2007), "Muscular Thin Films for Building Actuators and Powering Devices," Science **317** (5843), 1366–1370.
Guggenheim, James A, Jing Li, Thomas J. Allen, Richard J. Colchester, Sacha Noimark, Olumide Ogunlade, Ivan P. Parkin, Ioannis Papakonstantinou, Adrien E. Desjardins, Edward Z. Zhang, and Paul C. Beard (2017), "Ultrasensitive plano-concave optical microresonators for ultrasound sensing," Nature Photonics **11** (11), 714–719.
Gujrati, Vipul, Jaya Prakash, Jaber Malekzadeh-Najafabadi, Andre Stiel, Uwe Klemm, Gabriele Mettenleiter, Michaela Aichler, Axel Walch, and Vasilis Ntziachristos (2019), "Bioengineered bacterial vesicles as biological nano-heaters for optoacoustic imaging," Nature Communications **10** (1), 1114, number: 1.
Hajireza, Parsin, Wei Shi, Kevan Bell, Robert J Paproski, and Roger J Zemp (2017), "Non-interferometric photoacoustic remote sensing microscopy," Light: Science & Applications **6** (6), e16278–e16278.
Haraguchi, Yuji, Tatsuya Shimizu, Tadashi Sasagawa, Hidekazu Sekine, Katsuhisa Sakaguchi, Tetsutaro Kikuchi, Waki Sekine, Sachiko Sekiya, Masayuki Yamato, Mitsuo Umezu, and Teruo Okano (2012), "Fabrication of functional three-dimensional tissues by stacking cell sheets in vitro," Nature Protocols **7** (5), 850–858.
Harrison, Tyler, Janaka C. Ranasinghesagara, Huihong Lu, Kory Mathewson, Andrew Walsh, and Roger J. Zemp (2009), "Combined photoacoustic and ultrasound biomicroscopy," Optics Express **17** (24), 22041, number: 24.
Haven, Nathaniel J M, Pradyumna Kedarisetti, Brendon S. Restall, and Roger J. Zemp (2020), "Reflective objective-based ultraviolet photoacoustic remote sensing virtual histopathology," Optics Letters **45** (2), 535.
He, Hailong, Christine Schönmann, Mathias Schwarz, Benedikt Hindelang, Andrei Berezhnoi, Susanne Annette Steimle-Grauer, Ulf Darsow, Juan Aguirre, and Vasilis Ntziachristos (2022), "Fast raster-scan optoacoustic mesoscopy enables assessment of human melanoma mi-

crovasculature in vivo," Nature Communications **13** (1), 2803.

Heintzmann, Rainer, and Christoph G. Cremer (1999), "Laterally modulated excitation microscopy: improvement of resolution by using a diffraction grating," (Stockholm, Sweden) pp. 185–196.

Hellwarth, Robert, and Paul Christensen (1974), "Nonlinear optical microscopic examination of structure in polycrystalline ZnSe," Optics Communications **12** (3), 318–322, number: 3.

Hong, Guosong, Alexander L. Antaris, and Hongjie Dai (2017), "Near-infrared fluorophores for biomedical imaging," Nature Biomedical Engineering **1** (1), 0010, number: 1.

Huh, Dongeun, Benjamin D. Matthews, Akiko Mammoto, Martin Montoya-Zavala, Hong Yuan Hsin, and Donald E. Ingber (2010), "Reconstituting organ-level lung functions on a chip," Science **328** (5986), 1662–1668.

Hui, Jie, Rui Li, Evan H. Phillips, Craig J. Goergen, Michael Sturek, and Ji Xin Cheng (2016), "Bond-selective photoacoustic imaging by converting molecular vibration into acoustic waves," Photoacoustics **4** (1), 11–21, number: 1 Publisher: Elsevier GmbH.

Jackson, Warren, and Nabil M. Amer (1980), "Piezoelectric photoacoustic detection: Theory and experiment," Journal of Applied Physics **51** (6), 3343–3353.

Jathoul, Amit P, Jan Laufer, Olumide Ogunlade, Bradley Treeby, Ben Cox, Edward Zhang, Peter Johnson, Arnold R. Pizzey, Brian Philip, Teresa Marafioti, Mark F. Lythgoe, R. Barbara Pedley, Martin A. Pule, and Paul Beard (2015), "Deep in vivo photoacoustic imaging of mammalian tissues using a tyrosinase-based genetic reporter," Nature Photonics **9** (4), 239–246, number: 4.

Jiang, Yan, Tyler Harrison, Janaka Ranasinghesagara, and Roger J. Zemp (2010), "Photoacoustic and high-frequency power Doppler ultrasound biomicroscopy: a comparative study," Journal of Biomedical Optics **15** (5), 056008.

Jiang, Yuanyuan, Felix Sigmund, Josefine Reber, Xosé Luís Deán-Ben, Sarah Glasl, Moritz Kneipp, Héctor Estrada, Daniel Razansky, Vasilis Ntziachristos, and Gil G. Westmeyer (2015), "Violacein as a genetically-controlled, enzymatically amplified and photobleaching-resistant chromophore for optoacoustic bacterial imaging," Scientific Reports **5** (1), 11048.

Jiao, Shuliang, Zhixing Xie, Hao F. Zhang, and Carmen A. Puliafito (2009), "Simultaneous multimodal imaging with integrated photoacoustic microscopy and optical coherence tomography," Optics Letters **34** (19), 2961.

Karlas, Angelos, Miguel A. Pleitez, Juan Aguirre, and Vasilis Ntziachristos (2021), "Optoacoustic imaging in endocrinology and metabolism," Nature Reviews Endocrinology **17** (6), 323–335.

Kellnberger, Stephan, Walter Assmann, Sebastian Lehrack, Sabine Reinhardt, Peter Thirolf, Daniel Queirós, George Sergiadis, Günther Dollinger, Katia Parodi, and Vasilis Ntziachristos (2016), "Ionoacoustic tomography of the proton Bragg peak in combination with ultrasound and optoacoustic imaging," Scientific Reports **6** (1), 29305.

Khuri-Yakub, Butrus T, and Ömer Oralkan (2011), "Capacitive micromachined ultrasonic transducers for medical imaging and therapy," Journal of Micromechanics and Microengineering **21** (5), 054004.

Kim, Jeesu, Sara Park, Yuhan Jung, Sunyeob Chang, Jinyong Park, Yumiao Zhang, Jonathan F. Lovell, and Chulhong Kim (2016), "Programmable Real-time Clinical Photoacoustic and Ultrasound Imaging System," Scientific Reports **6** (1), 35137.

Kim, Jongbeom, Jin Young Kim, Seungwan Jeon, Jin Woo Baik, Seong Hee Cho, and Chulhong Kim (2019), "Super-resolution localization photoacoustic microscopy using intrinsic red blood cells as contrast absorbers," Light: Science & Applications **8** (1), 103.

Kneipp, Moritz, Héctor Estrada, Antonella Lauri, Jake Turner, Vasilis Ntziachristos, Gil G. Westmeyer, and Daniel Razansky (2015), "Volumetric tracking of migratory melanophores during zebrafish development by optoacoustic microscopy," Mechanisms of Development **138**, 300–304.

Knieling, Ferdinand, Clemens Neufert, Arndt Hartmann, Jing Claussen, Alexander Urich, Cornelia Egger, Marcel Vetter, Sarah Fischer, Lukas Pfeifer, Alexander Hagel, Christian Kielisch, Rüdiger S. Görtz, Dane Wildner, Matthias Engel, Jens Röther, Wolfgang Uter, Jürgen Siebler, Raja Atreya, Wolfgang Rascher, Deike Strobel, Markus F. Neurath, and Maximilian J. Waldner (2017), "Multispectral Optoacoustic Tomography for Assessment of Crohn's Disease Activity," New England Journal of Medicine **376** (13), 1292–1294, number: 13.

Kruger, Robert A, and Pingyu Liu (1994), "Photoacoustic ultrasound: Pulse production and detection in 0.5% Liposyn," Medical Physics **21** (7), 1179–1184.

Krumholz, Arie, Daria M. Shcherbakova, Jun Xia, Lihong V. Wang, and Vladislav V. Verkhusha (2014), "Multicontrast photoacoustic in vivo imaging using near-infrared fluorescent proteins," Scientific Reports **4** (1), 3939, number: 1.

Kukačka, Jan, Stephan Metz, Christoph Dehner, Alexander Muckenhuber, Korbinian Paul-Yuan, Angelos Karlas, Eva Maria Fallenberg, Ernst Rummeny, Dominik Jüstel, and Vasilis Ntziachristos (2022), "Image processing improvements afford second-generation handheld optoacoustic imaging of breast cancer patients," Photoacoustics **26** (March), 10.1016/j.pacs.2022.100343, number: March.

Kunyansky, Leonid A (2007), "Explicit inversion formulae for the spherical mean Radon transform," Inverse Problems **23** (1), 373–383.

Lancaster, Madeline A, Magdalena Renner, Carol-Anne Martin, Daniel Wenzel, Louise S. Bicknell, Matthew E. Hurles, Tessa Homfray, Josef M. Penninger, Andrew P. Jackson, and Juergen A. Knoblich (2013), "Cerebral organoids model human brain development and microcephaly," Nature **501** (7467), 373–379.

Laufer, Jan, Ben Cox, Edward Zhang, and Paul Beard (2010), "Quantitative determination of chromophore concentrations from 2D photoacoustic images using a nonlinear model-based inversion scheme," Applied Optics **49** (8), 1219.

Laufer, Jan G, Edward Z. Zhang, Bradley E. Treeby, Benjamin T. Cox, Paul C. Beard, Peter Johnson, and Barbara Pedley (2012), "In vivo preclinical photoacoustic imaging of tumor vasculature development and therapy," Journal of Biomedical Optics **17** (5), 1.

Lee, Changho, Seunghoon Han, Sehui Kim, Mansik Jeon, Min Yong Jeon, Chulhong Kim, and Jeehyun Kim (2013), "Combined photoacoustic and optical coherence tomography using a single near-infrared supercontinuum laser source," Applied Optics **52** (9), 1824, number: 9.

Lee, Hwi Don, Jun Geun Shin, Hoon Hyun, Bong-Ahn Yu, and Tae Joong Eom (2018), "Label-free photoacoustic microscopy for in-vivo tendon imaging using a fiber-based pulse laser," Scientific Reports **8** (1), 4805, number: 1.

Lee, Hwidon, Markus R. Seeger, Norman Lippok, Seemantini K. Nadkarni, Gijs van Soest, and Brett E. Bouma (2022), "Nanosecond SRS Fiber Amplifier for Label-free Near-Infrared Photoacoustic Microscopy of Lipids," Photoacoustics **25**, 100331, publisher: Elsevier GmbH.

Lei, Zhao, Yun Zeng, Xiaofen Zhang, Xiaoyong Wang, and Gang Liu (2020), "Photoacoustic reporter genes for non-invasive molecular imaging and theranostics," Journal of Innovative Optical Health Sciences **13** (03), 2030005.

Li, Hao, Biqin Dong, Zhen Zhang, Hao F. Zhang, and Cheng Sun (2014), "A transparent broadband ultrasonic detector based on an optical micro-ring resonator for photoacoustic microscopy," Scientific Reports **4** (1), 4496, number: 1.

Li, Li, Roger J. Zemp, Gina Lungu, George Stoica, and Lihong V. Wang (2006), "Imaging of gene expression in vivo with photoacoustic tomography," (San Jose, CA) p. 608608.

Li, Li, Roger J. Zemp, Gina Lungu, George Stoica, and Lihong V. Wang (2007), "Photoacoustic imaging of lacZ gene expression in vivo," Journal of Biomedical Optics **12** (2), 020504.

Li, Yan, Alex Forbrich, Jiahui Wu, Peng Shao, Robert E. Campbell, and Roger Zemp (2016), "Engineering Dark Chromoprotein Reporters for Photoacoustic Microscopy and FRET Imaging," Scientific Reports **6** (1), 22129, number: 1.

Li, Yan, Riqiang Lin, Chengbo Liu, Jianhua Chen, Huadong Liu, Rongqin Zheng, Xiaojing Gong, and Liang Song (2018), "In vivo photoacoustic/ultrasonic dual-modality endoscopy with a miniaturized full field-of-view catheter," Journal of Biophotonics **11** (10), 1–8, number: 10 ISBN: 2017041315312.

Liao, Lun-De, Meng-Lin Li, Hsin-Yi Lai, Yen-Yu I. Shih, Yu-Chun Lo, Siny Tsang, Paul Chang-Po Chao, Chin-Teng Lin, Fu-Shan Jaw, and You-Yin Chen (2010), "Imaging brain hemodynamic changes during rat forepaw electrical stimulation using functional photoacoustic microscopy," NeuroImage **52** (2), 562–570, number: 2.

Lin, Hsiao-Chun Amy, Andrei Chekkoury, Murad Omar, Tobias Schmitt-Manderbach, Benno Koberstein-Schwarz, Timo Mappes, Hernán López-Schier, Daniel Razansky, and Vasilis Ntziachristos (2015), "Selective plane illumination optical and optoacoustic microscopy for postembryonic imaging: Selective plane illumination optical and optoacoustic microscopy for postembryonic imaging," Laser & Photonics Reviews **9** (5), L29–L34.

Lin, Li, Peng Hu, Xin Tong, Shuai Na, Rui Cao, Xiaoyun Yuan, David C. Garrett, Junhui Shi, Konstantin Maslov, and Lihong V. Wang (2021), "High-speed three-dimensional photoacoustic computed tomography for preclinical research and clinical translation," Nature Communications **12** (1), 1–10, number: 1 Publisher: Springer US.

Liu, Xiaojing, Tan Liu, Rong Wen, Yiwen Li, Carmen A. Puliafito, Hao F. Zhang, and Shuliang Jiao (2015), "Optical coherence photoacoustic microscopy for in vivo multimodal retinal imaging," Optics Letters **40** (7), 1370.

Liu, Xiaojing, Rong Wen, Yiwen Li, and Shuliang Jiao (2016), "Optical coherence photoacoustic microscopy (OC-PAM) with an intensity-modulated continuous-wave broadband light source," Journal of Optics **18** (6), 064001.

Lu, Qiang-Bing, Tuo Liu, Lei Ding, Ming-Hui Lu, Jie Zhu, and Yan-Feng Chen (2020), "Probing the Spatial Impulse Response of Ultrahigh-Frequency Ultrasonic Transducers with Photoacoustic Waves," Physical Review Applied **14** (3), 034026.

Lutzweiler, Christian, and Daniel Razansky (2013), "Optoacoustic Imaging and Tomography: Reconstruction Approaches and Outstanding Challenges in Image Performance and Quantification," Sensors **13** (6), 7345–7384.

Manwar, Rayyan, Karl Kratkiewicz, and Kamran Avanaki (2020), "Overview of Ultrasound Detection Technologies for Photoacoustic Imaging," Micromachines **11** (7), 692.

Maslov, Konstantin, Gheorghe Stoica, and Lihong V. Wang (2005), "In vivo dark-field reflection-mode photoacoustic microscopy," Optics Letters **30** (6), 625, number: 6.

Maslov, Konstantin, Hao F. Zhang, Song Hu, and Lihong V. Wang (2008), "Optical-resolution photoacoustic microscopy for in vivo imaging of single capillaries," Optics Letters **33** (9), 929.

Maswadi, Saher M, Bennett L. Ibey, Caleb C. Roth, Dmitri A. Tsyboulski, Hope T. Beier, Randolph D. Glickman, and Alexander A. Oraevsky (2016), "All-optical optoacoustic microscopy based on probe beam deflection technique," Photoacoustics **4** (3), 91–101, number: 3.

Maxwell, Adam, Sheng-Wen Huang, Tao Ling, Jin-Sung Kim, Shai Ashkenazi, and L. Jay Guo (2008), "Polymer Microring Resonators for High-Frequency Ultrasound Detection and Imaging," IEEE Journal of Selected Topics in Quantum Electronics **14** (1), 191–197.

Mishra, Kanuj, Juan Pablo Fuenzalida-Werner, Vasilis Ntziachristos, and Andre C. Stiel (2019), "Photocontrollable Proteins for Optoacoustic Imaging," Analytical Chemistry **91** (9), 5470–5477.

Mishra, Kanuj, Juan Pablo Fuenzalida-Werner, Francesca Pennacchietti, Robert Janowski, Andriy Chmyrov, Yuanhui Huang, Christian Zakian, Uwe Klemm, Ilaria Testa, Dierk Niessing, Vasilis Ntziachristos, and Andre C. Stiel (2022), "Genetically encoded photo-switchable molecular sensors for optoacoustic and super-resolution imaging," Nature Biotechnology **40** (4), 598–605, number: 4.

Mishra, Kanuj, Mariia Stankevych, Juan Pablo Fuenzalida-Werner, Simon Grassmann, Vipul Gujrati, Yuanhui Huang, Uwe Klemm, Veit R. Buchholz, Vasilis Ntziachristos, and Andre C. Stiel (2020), "Multiplexed whole-animal imaging with reversibly switchable optoacoustic proteins," Science Advances **6** (24), eaaz6293, number: 24.

Märk, Julia, Asja Wagener, Edward Zhang, and Jan Laufer (2017), "Photoacoustic pump-probe tomography of fluorophores in vivo using interleaved image acquisition for motion suppression," Scientific Reports **7** (1), 40496.

Nau, T, C. Schönmann, B. Hindelang, L. Riobo, A. Doll, S. Schneider, L. Englert, H. He, T. Biedermann, U. Darsow, F. Lauffer, V. Ntziachristos, and J. Aguirre (2023), "Raster-scanning optoacoustic mesoscopy biomarkers for atopic dermatitis skin lesions," Photoacoustics **31**, 100513.

Nteroli, Gianni, Manoj K. Dasa, Giulia Messa, Stella Koutsikou, Magalie Bondu, Peter M. Moselund, Christos Markos, Ole Bang, Adrian Podoleanu, and Adrian Bradu (2022), "Two octaves spanning photoacoustic microscopy," Scientific Reports **12** (1), 10590.

Ntziachristos, Vasilis (2010), "Going deeper than microscopy: the optical imaging frontier in biology," Nature Methods **7** (8), 603–614, number: 8.

Ntziachristos, Vasilis (2024), "Addressing unmet clinical need with optoacoustic imaging," Nature Reviews Bioengineering 10.1038/s44222-024-00242-w.

Ntziachristos, Vasilis, Jorge Ripoll, Lihong V Wang, and Ralph Weissleder (2005), "Looking and listening to light: the evolution of whole-body photonic imaging," Nature Biotechnology **23** (3), 313–320, number: 3.

Nuster, Robert, Paul Slezak, and Guenther Paltauf (2014), "High resolution three-dimensional photoacoustic tomography with CCD-camera based ultrasound detection," Biomedical Optics Express **5** (8), 2635, number: 8.

Olsen, Richard G, and James C. Lin (1983), "Acoustical imaging of a model of a human hand using pulsed microwave irradiation," Bioelectromagnetics **4** (4), 397–400.

Omar, Murad, Juan Aguirre, and Vasilis Ntziachristos (2019), "Optoacoustic mesoscopy for biomedicine," Nature Biomedical Engineering **3** (5), 354–370, publisher: Springer US.

Omar, Murad, Mathias Schwarz, Dominik Soliman, Panagiotis Symvoulidis, and Vasilis Ntziachristos (2015), "Pushing the Optical Imaging Limits of Cancer with Multi-Frequency-Band Raster-Scan Optoacoustic Mesoscopy (RSOM)," Neoplasia **17** (2), 208–214.

Oraevsky, AA, B. Clingman, J. Zalev, A.T. Stavros, W.T. Yang, and J.R. Parikh (2018), "Clinical optoacoustic imaging combined with ultrasound for coregistered functional and anatomical mapping of breast tumors," Photoacoustics **12**, 30–45.

Oraevsky, Alexander A, Steven L. Jacques, and Frank K. Tittel (1993), "Determination of tissue optical properties by piezoelectric detection of laser-induced stress waves," (Los Angeles, CA) p. 86.

Oraevsky, Alexander A, and Alexander A. Karabutov (2000), "Ultimate sensitivity of time-resolved optoacoustic detection," (San Jose, CA) pp. 228–239.

Orofino, DP, and P.C. Pedersen (1993), "Efficient angular spectrum decomposition of acoustic sources. I. Theory," IEEE Transactions on Ultrasonics, Ferroelectrics and Frequency Control **40** (3), 238–249, number: 3.

Paltauf, G, J. A. Viator, S. A. Prahl, and S. L. Jacques (2002), "Iterative reconstruction algorithm for optoacoustic imaging," The Journal of the Acoustical Society of America **112** (4), 1536–1544.

Patel, C K N, and A. C. Tam (1981), "Pulsed optoacoustic spectroscopy of condensed matter," Reviews of Modern Physics **53** (3), 517–550.

Pleitez, Miguel A, Asrar Ali Khan, Alice Soldà, Andriy Chmyrov, Josefine Reber, Francesca Gasparin, Markus R. Seeger, Benedikt Schätz, Stephan Herzig, Marcel Scheideler, and Vasilis Ntziachristos (2020), "Label-free metabolic imaging by mid-infrared optoacoustic microscopy in living cells," Nature Biotechnology **38** (3), 293–296, number: 3 Publisher: Springer US.

Preisser, Stefan, Wolfgang Rohringer, Mengyang Liu, Christian Kollmann, Stefan Zotter, Balthasar Fischer, and Wolfgang Drexler (2016), "All-optical highly sensitive akinetic sensor for ultrasound detection and photoacoustic imaging," Biomedical Optics Express **7** (10), 4171.

Rao, Bin, Florentina Soto, Daniel Kerschensteiner, and Lihong V. Wang (2014), "Integrated photoacoustic, confocal, and two-photon microscope," Journal of Biomedical Optics **19** (3), 036002, number: 3.

Razansky, Daniel, Martin Distel, Claudio Vinegoni, Rui Ma, Norbert Perrimon, Reinhard W. Köster, and Vasilis Ntziachristos (2009), "Multispectral opto-acoustic tomography of deep-seated fluorescent proteins in vivo," Nature Photonics **3** (7), 412–417, number: 7.

Read, AW (1968), "The measurement of vibrational relaxation times using the optic-acoustic effect," Advances in Molecular Relaxation Processes **1** (3), 257–272.

Reber, Josefine, Monja Willershäuser, Angelos Karlas, Korbinian Paul-Yuan, Gael Diot, Daniela Franz, Tobias Fromme, Saak V. Ovsepian, Nicolas Bézière, Elena Dubikovskaya, Dimitrios C. Karampinos, Christina Holzapfel, Hans Hauner, Martin Klingenspor, and Vasilis Ntziachristos (2018), "Non-invasive Measurement of Brown Fat Metabolism Based on Optoacoustic Imaging of Hemoglobin Gradients," Cell Metabolism **27** (3), 689–701.e4, number: 3.

Rebling, Johannes, Héctor Estrada, Sven Gottschalk, Gali Sela, Michael Zwack, Georg Wissmeyer, Vasilis Ntziachristos, and Daniel Razansky (2018), "Dual-wavelength hybrid optoacoustic-ultrasound biomicroscopy for functional imaging of large-scale cerebral vascular networks," Journal of Biophotonics **11** (9), e201800057, number: 9.

Regensburger, Adrian P, Lina M. Fonteyne, Jörg Jüngert, Alexandra L. Wagner, Teresa Gerhalter, Armin M. Nagel, Rafael Heiss, Florian Flenkenthaler, Matthias Qurashi, Markus F. Neurath, Nikolai Klymiuk, Elisabeth Kemter, Thomas Fröhlich, Michael Uder, Joachim Woelfle, Wolfgang Rascher, Regina Trollmann, Eckhard Wolf, Maximilian J. Waldner, and Ferdinand Knieling (2019), "Detection of collagens by multispectral optoacoustic tomography as an imaging biomarker for Duchenne muscular dystrophy," Nature Medicine **25** (12), 1905–1915, number: 12.

Roberts, Sheryl, Markus Seeger, Yuanyuan Jiang, Anurag Mishra, Felix Sigmund, Anja Stelzl, Antonella Lauri, Panagiotis Symvoulidis, Hannes Rolbieski, Matthias Preller, X. Luís Deán-Ben, Daniel Razansky, Tanja Orschmann, Sabrina C. Desbordes, Paul Vetschera, Thorsten Bach, Vasilis Ntziachristos, and Gil G. Westmeyer (2018), "Calcium Sensor for Photoacoustic Imaging," Journal of the American Chemical Society **140** (8), 2718–2721, number: 8.

Rohringer, Wolfgang, Stefan Preißer, Mengyang Liu, Stefan Zotter, Zhe Chen, Boris Hermann, Harald Sattmann, Balthasar Fischer, and Wolfgang Drexler (2016), "All-optical highly sensitive broadband ultrasound sensor without any deformable parts for photoacoustic imaging," (San Francisco, California, United States) p. 970815.

Ronaldson-Bouchard, Kacey, Diogo Teles, Keith Yeager, Daniel Naveed Tavakol, Yimu Zhao, Alan Chramiec, Somnath Tagore, Max Summers, Sophia Stylianos, Manuel Tamargo, Busub Marcus Lee, Susan P. Halligan, Erbil Hasan Abaci, Zongyou Guo, Joanna Jacków, Alberto Pappalardo, Jerry Shih, Rajesh K. Soni, Shivam Sonar, Carrie German, Angela M. Christiano, Andrea Califano, Karen K. Hirschi, Christopher S. Chen, Andrzej Przekwas, and Gordana Vunjak-Novakovic (2022), "A multi-organ chip with matured tissue niches linked by vascular flow," Nature Biomedical Engineering **6** (4), 351–371.

Rosencwaig, A (1973), "Photoacoustic Spectroscopy of Biological Materials," Science **181** (4100), 657–658.

Rosencwaig, Allan, and Allen Gersho (1976), "Theory of the photoacoustic effect with solids," Journal of Applied Physics **47** (1), 64–69.

Rosenthal, Amir, Stephan Kellnberger, Dmitry Bozhko, Andrei Chekkoury, Murad Omar, Daniel Razansky, and

Vasilis Ntziachristos (2014a), "Sensitive interferometric detection of ultrasound for minimally invasive clinical imaging applications: Sensitive interferometric detection of ultrasound for clinical imaging applications," Laser & Photonics Reviews **8** (3), 450–457.

Rosenthal, Amir, Vasilis Ntziachristos, and Daniel Razansky (2011a), "Calibration of ultrasonic sensors using optoacoustics," (San Francisco, California, USA) p. 78992L.

Rosenthal, Amir, Vasilis Ntziachristos, and Daniel Razansky (2011b), "Model-based optoacoustic inversion with arbitrary-shape detectors," Medical Physics **38** (7), 4285–4295, number: 7.

Rosenthal, Amir, Murad Omar, Héctor Estrada, Stephan Kellnberger, Daniel Razansky, and Vasilis Ntziachristos (2014b), "Embedded ultrasound sensor in a silicon-on-insulator photonic platform," Applied Physics Letters **104** (2), 021116.

Rosenthal, Amir, Daniel Razansky, and Vasilis Ntziachristos (2011c), "High-sensitivity compact ultrasonic detector based on a pi-phase-shifted fiber Bragg grating," Optics Letters **36** (10), 1833, number: 10.

Ruan, Qing, Lei Xi, Sanford L. Boye, Song Han, Zhi J. Chen, William W. Hauswirth, Alfed S. Lewin, Michael E. Boulton, Brian K. Law, Wen G. Jiang, Huabei Jiang, and Jun Cai (2013), "Development of an anti-angiogenic therapeutic model combining scAAV2-delivered siRNAs and noninvasive photoacoustic imaging of tumor vasculature development," Cancer Letters **332** (1), 120–129, number: 1.

Rust, Michael J, Mark Bates, and Xiaowei Zhuang (2006), "Sub-diffraction-limit imaging by stochastic optical reconstruction microscopy (STORM)," Nature Methods **3** (10), 793–796.

Sato, Toshiro, and Hans Clevers (2013), "Growing Self-Organizing Mini-Guts from a Single Intestinal Stem Cell: Mechanism and Applications," Science **340** (6137), 1190–1194.

Schwarz, Mathias, Andreas Buehler, Juan Aguirre, and Vasilis Ntziachristos (2016), "Three-dimensional multispectral optoacoustic mesoscopy reveals melanin and blood oxygenation in human skin *in vivo*," Journal of Biophotonics **9** (1-2), 55–60.

Seeger, Markus, Christoph Dehner, Dominik Jüstel, and Vasilis Ntziachristos (2021), "Label-free concurrent 5-modal microscopy (Co5M) resolves unknown spatiotemporal processes in wound healing," Communications Biology **4** (1), 10.1038/s42003-021-02573-5, number: 1 Publisher: Springer US.

Seeger, Markus, Angelos Karlas, Dominik Soliman, Jaroslav Pelisek, and Vasilis Ntziachristos (2016), "Multimodal optoacoustic and multiphoton microscopy of human carotid atheroma," Photoacoustics **4** (3), 102–111, number: 3 Publisher: Elsevier GmbH.

Seeger, Markus, Dominik Soliman, Juan Aguirre, Gael Diot, Jakob Wierzbowski, and Vasilis Ntziachristos (2020), "Pushing the boundaries of optoacoustic microscopy by total impulse response characterization," Nature Communications **11** (1), 1–13, publisher: Springer US.

Seeger, Markus, Gil Westmeyer, and Vasilis Ntziachristos (2019), "In vivo hybrid microscopy of small model organisms," Optics InfoBase Conference Papers **Part F142-**, 10–13, iSBN: 9781557528209.

Shi, Junhui, Terence T. W. Wong, Yun He, Lei Li, Ruiying Zhang, Christopher S. Yung, Jeeseong Hwang, Konstantin Maslov, and Lihong V. Wang (2019), "High-resolution, high-contrast mid-infrared imaging of fresh biological samples with ultraviolet-localized photoacoustic microscopy," Nature Photonics **13** (9), 609–615, number: 9.

Shimomura, Osamu, Frank H. Johnson, and Yo Saiga (1962), "Extraction, Purification and Properties of Aequorin, a Bioluminescent Protein from the Luminous Hydromedusan,Aequorea," Journal of Cellular and Comparative Physiology **59** (3), 223–239, number: 3.

Shnaiderman, Rami, Georg Wissmeyer, Markus Seeger, Dominik Soliman, Hector Estrada, Daniel Razansky, Amir Rosenthal, and Vasilis Ntziachristos (2017), "Fiber interferometer for hybrid optical and optoacoustic intravital microscopy," Optica **4** (10), 1180, number: 10.

Shnaiderman, Rami, Georg Wissmeyer, Okan Ülgen, Qutaiba Mustafa, Andriy Chmyrov, and Vasilis Ntziachristos (2020), "A submicrometre silicon-on-insulator resonator for ultrasound detection," Nature **585** (7825), 372–378, number: 7825 Publisher: Springer US.

Sibarita, Jean-Baptiste (2005), "Deconvolution Microscopy," in *Microscopy Techniques*, Vol. 95, edited by Jens Rietdorf (Springer Berlin Heidelberg, Berlin, Heidelberg) pp. 201–243, series Title: Advances in Biochemical Engineering/Biotechnology.

Soliman, Dominik, George J. Tserevelakis, Murad Omar, and Vasilis Ntziachristos (2015a), "Combining microscopy with mesoscopy using optical and optoacoustic label-free modes," Scientific Reports **5** (1), 12902, number: 1.

Soliman, Dominik, George J. Tserevelakis, Murad Omar, and Vasilis Ntziachristos (2015b), "Hybrid label-free multiphoton and optoacoustic microscopy (MPOM)," in *Opto-Acoustic Methods and Applications in Biophotonics II* (OSA, Munich) p. 953908.

Soliman, Dominik, George J. Tserevelakis, Murad Omar, and Vasilis Ntziachristos (2016), "Combined label-free optical and optoacoustic imaging of model organisms at mesoscopy and microscopy resolutions," (San Francisco, California, United States) p. 97083B.

Song, Wei, Qing Wei, Wenzhong Liu, Tan Liu, Ji Yi, Nader Sheibani, Amani A. Fawzi, Robert A. Linsenmeier, Shuliang Jiao, and Hao F. Zhang (2014), "A combined method to quantify the retinal metabolic rate of oxygen using photoacoustic ophthalmoscopy and optical coherence tomography," Scientific Reports **4** (1), 6525, number: 1.

Song, Wei, Qiang Xu, Yang Zhang, Yang Zhan, Wei Zheng, and Liang Song (2016), "Fully integrated reflection-mode photoacoustic, two-photon, and second harmonic generation microscopy in vivo," Scientific Reports **6** (August), 1–8, number: August Publisher: Nature Publishing Group.

Stiel, Andre C, Xosé Luís Deán-Ben, Yuanyuan Jiang, Vasilis Ntziachristos, Daniel Razansky, and Gil G. Westmeyer (2015), "High-contrast imaging of reversibly switchable fluorescent proteins via temporally unmixed multispectral optoacoustic tomography," Optics Letters **40** (3), 367, number: 3.

Stritzker, Jochen, Lorenz Kirscher, Miriam Scadeng, Nikolaos C. Deliolanis, Stefan Morscher, Panagiotis Symvoulidis, Karin Schaefer, Qian Zhang, Lisa Buckel, Michael Hess, Ulrike Donat, William G. Bradley, Vasilis Ntziachristos, and Aladar A. Szalay (2013), "Vaccinia virus-mediated melanin production allows MR and optoacoustic deep tissue imaging and laser-induced thermotherapy of cancer," Proceedings of the National Academy of Sciences **110** (9), 3316–3320.

Strohm, Eric M, Elizabeth S.L. Berndl, and Michael C. Kolios (2013), "High frequency label-free photoacoustic microscopy of single cells," Photoacoustics **1** (3-4), 49–53, number: 3-4.

Strohm, Eric M, Michael J. Moore, and Michael C. Kolios (2016), "High resolution ultrasound and photoacoustic imaging of single cells," Photoacoustics **4** (1), 36–42, number: 1.

Stylogiannis, Antonios, Ludwig Prade, Sarah Glasl, Qutaiba Mustafa, Christian Zakian, and Vasilis Ntziachristos (2022), "Frequency wavelength multiplexed optoacoustic tomography," Nature Communications **13** (1), 4448.

Subochev, Pavel, Alexey Katichev, Andrey Morozov, Anna Orlova, Vladislav Kamensky, and Ilya Turchin (2012), "Simultaneous photoacoustic and optically mediated ultrasound microscopy: phantom study," Optics Letters **37** (22), 4606.

Subochev, Pavel, Anna Orlova, Marina Shirmanova, Anna Postnikova, and Ilya Turchin (2015), "Simultaneous photoacoustic and optically mediated ultrasound microscopy: an in vivo study," Biomedical Optics Express **6** (2), 631.

Sun, Aihui, Heng Guo, Qi Gan, Lei Yang, Qiang Liu, and Lei Xi (2020), "Evaluation of visible NIR-I and NIR-II light penetration for photoacoustic imaging in rat organs," Optics Express **28** (6), 9002, number: 6.

Taboada, Carlos, Jesse Delia, Maomao Chen, Chenshuo Ma, Xiaorui Peng, Xiaoyi Zhu, Laiming Jiang, Tri Vu, Qifa Zhou, Junjie Yao, Lauren O'Connell, and Sönke Johnsen (2022), "Glassfrogs conceal blood in their liver to maintain transparency," Science **378** (6626), 1315–1320, number: 6626.

Taruttis, Adrian, and Vasilis Ntziachristos (2015), "Advances in real-time multispectral optoacoustic imaging and its applications," Nature Photonics **9** (4), 219–227, number: 4.

Treeby, Bradley E, and Benjamin T. Cox (2009), "Fast tissue-realistic models of photoacoustic wave propagation for homogeneous attenuating media," (San Jose, CA) p. 717716.

Tserevelakis, George J, Stella Avtzi, Miltiadis K. Tsilimbaris, and Giannis Zacharakis (2017), "Delineating the anatomy of the ciliary body using hybrid optical and photoacoustic imaging," Journal of Biomedical Optics **22** (6), 060501, number: 6.

Tserevelakis, George J, Kostas G. Mavrakis, Danai Pantazopoulou, Eleni Lagoudaki, Efstathios Detorakis, and Giannis Zacharakis (2020), "Hybrid autofluorescence and photoacoustic label-free microscopy for the investigation and identification of malignancies in ocular biopsies," Optics Letters **45** (20), 5748, number: 20.

Tserevelakis, George J, Michalis Pavlidis, Athanasios Samaras, Georgios D. Barmparis, Kostas G. Mavrakis, Ioannis Draganidis, Athanasios Oikonomou, Eleftheria Fanouraki, Giorgos P. Tsironis, and Giannis Zacharakis (2022), "Hybrid confocal fluorescence and photoacoustic microscopy for the label-free investigation of melanin accumulation in fish scales," Scientific Reports **12** (1), 7173, number: 1.

Tserevelakis, George J, Dominik Soliman, Murad Omar, and Vasilis Ntziachristos (2014), "Hybrid multiphoton and optoacoustic microscope," Optics Letters **39** (7), 1819, number: 7.

Tserevelakis, George J, Margarita Tsagkaraki, and Giannis Zacharakis (2016), "Hybrid photoacoustic and optical imaging of pigments in vegetative tissues," Journal of Microscopy **263** (3), 300–306, number: 3.

Uluç, Nasire, Sarah Glasl, Francesca Gasparin, Tao Yuan, Hailong He, Dominik Jüstel, Miguel A. Pleitez, and Vasilis Ntziachristos (2024), "Non-invasive measurements of blood glucose levels by time-gating mid-infrared optoacoustic signals," Nature Metabolism 10.1038/s42255-024-01016-9.

Upputuri, Paul Kumar, and Manojit Pramanik (2019), "Photoacoustic imaging in the second near-infrared window: a review," Journal of Biomedical Optics **24** (04), 1.

Vetschera, Paul, Benno Koberstein-Schwarz, Tobias Schmitt-Manderbach, Christian Dietrich, Wibke Hellmich, Andrei Chekkoury, Panagiotis Symvoulidis, Josefine Reber, Gil Westmeyer, Hernán López-Schier, Murad Omar, and Vasilis Ntziachristos (2023), "Beyond Early Development: Observing Zebrafish over 6 Weeks with Hybrid Optical and Optoacoustic Imaging," Laser & Photonics Reviews **17** (7), 2200846, number: 7.

Visscher, Mirjam, Miguel A. Pleitez, Kim Van Gaalen, Ingeborg M. Nieuwenhuizen-Bakker, Vasilis Ntziachristos, and Gijs Van Soest (2022), "Label-free analytic histology of carotid atherosclerosis by mid-infrared optoacoustic microscopy," Photoacoustics **26**, 100354.

Wada, Katsuya, Tsutomu Masujima, Hisanobu Yoshida, and Hideo Imai (1986), "Photoacoustic microscopy for the analysis of peroxidase activity in a biological tissue." Chemical and Pharmaceutical Bulletin **34** (4), 1834–1836.

Wada, Katsuya, Tsutomu Masujima, Hisanobu Yoshida, Teruo Murakami, Noboru Yata, and Hideo Imai (1985), "Laser photoacoustic microscopy for the determination of dye on a solid biopolymer," Chemical and Pharmaceutical Bulletin **33** (3), 1316–1319, number: 3.

Wang, Lidai, Konstantin Maslov, and Lihong V. Wang (2013), "Single-cell label-free photoacoustic flowoxigraphy in vivo," Proceedings of the National Academy of Sciences **110** (15), 5759–5764.

Wang, Lihong V, and Song Hu (2012), "Photoacoustic tomography: In vivo imaging from organelles to organs," Science **335** (6075), 1458–1462.

Wang, Lihong V, and Hsin-i Wu (2007), *Biomedical optics: principles and imaging* (Wiley-Interscience, Hoboken, N.J) oCLC: ocm71427127.

Wang, Yu, Song Hu, Konstantin Maslov, Yu Zhang, Younan Xia, and Lihong V. Wang (2011), "In vivo integrated photoacoustic and confocal microscopy of hemoglobin oxygen saturation and oxygen partial pressure," Optics Letters **36** (7), 1029, number: 7.

Weber, Judith, Paul C Beard, and Sarah E Bohndiek (2016), "Contrast agents for molecular photoacoustic imaging," Nature Methods **13** (8), 639–650, number: 8.

Wei, Heming, and Sridhar Krishnaswamy (2017), "Polymer micro-ring resonator integrated with a fiber ring laser for ultrasound detection," Optics Letters **42** (13), 2655.

Weissleder, R, M Simonova, A Bogdanova, S Bredow, W S Enochs, and A Bogdanov (1997), "MR imaging and scintigraphy of gene expression through melanin induction." Radiology **204** (2), 425–429, number: 2.

Westerveld, Wouter J, Md. Mahmud-Ul-Hasan, Rami Shnaiderman, Vasilis Ntziachristos, Xavier Rottenberg, Simone Severi, and Veronique Rochus (2021), "Sensitive, small, broadband and scalable optomechanical ultrasound sensor in silicon photonics," Nature Photonics **15** (5), 341–345.

Westervelt, Peter J, and Richard S. Larson (1973), "Laser-excited broadside array," The Journal of the Acoustical Society of America **54** (1), 121–122, number: 1.

Winkler, Amy M, Konstantin Maslov, and Lihong V. Wang (2013), "Noise-equivalent sensitivity of photoacoustics," Journal of Biomedical Optics **18** (9), 097003, number: 9.

Wissmeyer, Georg, Miguel A. Pleitez, Amir Rosenthal, and Vasilis Ntziachristos (2018), "Looking at sound: optoacoustics with all-optical ultrasound detection," Light: Science and Applications **7** (1), 10.1038/s41377-018-0036-7, number: 1 Publisher: Springer US.

Wissmeyer, Georg, Dominik Soliman, Rami Shnaiderman, Amir Rosenthal, and Vasilis Ntziachristos (2016), "All-optical optoacoustic microscope based on wideband pulse interferometry," Optics Letters **41** (9), 1953, number: 9.

Wong, Y H, R. L. Thomas, and G. F. Hawkins (1978), "Surface and subsurface structure of solids by laser photoacoustic spectroscopy," Applied Physics Letters **32** (9), 538–539.

Wygant, IO, Xuefeng Zhuang, D.T. Yeh, O. Oralkan, A.S. Ergun, M. Karaman, and B.T. Khuri-Yakub (2008), "Integration of 2D CMUT arrays with front-end electronics for volumetric ultrasound imaging," IEEE Transactions on Ultrasonics, Ferroelectrics and Frequency Control **55** (2), 327–342.

Xiang, Liangzhong, Shanshan Tang, Moiz Ahmad, and Lei Xing (2016), "High Resolution X-ray-Induced Acoustic Tomography," Scientific Reports **6** (1), 26118, number: 1.

Xiao, Meichun, Cuixia Dai, Lin Li, Chuanqing Zhou, and Fenghua Wang (2020), "Evaluation of Retinal Pigment Epithelium and Choroidal Neovascularization in Rats Using Laser-Scanning Optical-Resolution Photoacoustic Microscopy," Ophthalmic Research **63** (3), 271–283, number: 3.

Xu, Minghua, and Lihong V. Wang (2003), "Analytic explanation of spatial resolution related to bandwidth and detector aperture size in thermoacoustic or photoacoustic reconstruction," Physical Review E **67** (5), 056605, number: 5.

Xu, Minghua, and Lihong V. Wang (2005), "Universal back-projection algorithm for photoacoustic computed tomography," Physical Review E Statistical, Nonlinear, and Soft Matter Physics **71** (1), 1–7.

Yao, Da-Kang, Konstantin Maslov, Kirk K. Shung, Qifa Zhou, and Lihong V. Wang (2010), "In vivo label-free photoacoustic microscopy of cell nuclei by excitation of DNA and RNA," Optics Letters **35** (24), 4139.

Yao, Junjie, Andrii A Kaberniuk, Lei Li, Daria M Shcherbakova, Ruiying Zhang, Lidai Wang, Guo Li, Vladislav V Verkhusha, and Lihong V Wang (2016), "Multiscale photoacoustic tomography using reversibly switchable bacterial phytochrome as a near-infrared photochromic probe," Nature Methods **13** (1), 67–73, number: 1.

Yu Wang,, Konstantin Maslov, Chulhong Kim, Song Hu, and Lihong V Wang (2010), "Integrated Photoacoustic and Fluorescence Confocal Microscopy," IEEE Transactions on Biomedical Engineering **57** (10), 2576–2578, number: 10.

Zalev, Jason, Lisa M. Richards, Bryan A. Clingman, Jeff Harris, Edgar Cantu, Gisela L. G. Menezes, Carlos A. Avila, Allison Bertrand, Xavier R. Saenz, Steve C. Miller, Alexander A. Oraevsky, and Michael C. Kolios (2019), "Optoacoustic imaging of relative blood oxygen saturation and total hemoglobin for breast cancer diagnosis," Journal of Biomedical Optics **24** (12), 1.

Zanelli, Claudio I, and Samuel M. Howard (2006), "Schlieren metrology for high frequency medical ultrasound," Ultrasonics **44**, e105–e107.

Zhang, Chi, Ya-Jian Cheng, Junjie Chen, Samuel Wickline, and Lihong V. Wang (2012a), "Label-free photoacoustic microscopy of myocardial sheet architecture," Journal of Biomedical Optics **17** (6), 060506, number: 6.

Zhang, Chi, Konstantin I. Maslov, Junjie Yao, and Lihong V. Wang (2012b), "In vivo photoacoustic microscopy with 7.6-µm axial resolution using a commercial 125-MHz ultrasonic transducer," Journal of Biomedical Optics **17** (11), 1, number: 11.

Zhang, Chi, Yu Shrike Zhang, Da-Kang Yao, Younan Xia, and Lihong V. Wang (2013), "Label-free photoacoustic microscopy of cytochromes," Journal of Biomedical Optics **18** (2), 020504, number: 2.

Zhang, E Z, J G Laufer, R B Pedley, and P C Beard (2009), "In vivo high-resolution 3D photoacoustic imaging of superficial vascular anatomy," Physics in Medicine and Biology **54** (4), 1035–1046, number: 4.

Zhang, Edward, Jan Laufer, and Paul Beard (2008), "Backward-mode multiwavelength photoacoustic scanner using a planar Fabry-Perot polymer film ultrasound sensor," Applied Optics **47** (4), 561–577, number: 4.

Zhang, Hao F, Konstantin Maslov, George Stoica, and Lihong V. Wang (2006), "Functional photoacoustic microscopy for high-resolution and noninvasive in vivo imaging," Nature Biotechnology **24** (7), 848–851, number: 7.

Zhang, Hao F, Jing Wang, Qing Wei, Tan Liu, Shuliang Jiao, and Carmen A. Puliafito (2010a), "Collecting back-reflected photons in photoacoustic microscopy," Optics Express **18** (2), 1278, number: 2.

Zhang, Wei, Yanxiu Li, Van Phuc Nguyen, Ziyi Huang, Zhipeng Liu, Xueding Wang, and Yannis M. Paulus (2018), "High-resolution, in vivo multimodal photoacoustic microscopy, optical coherence tomography, and fluorescence microscopy imaging of rabbit retinal neovascularization," Light: Science & Applications **7** (1), 103, number: 1.

Zhang, Xiangyang, Minshan Jiang, Amani A. Fawzi, Xiang Li, K. Kirk Shung, Carmen A. Puliafito, Hao F. Zhang, and Shuliang Jiao (2010b), "Simultaneous dual molecular contrasts provided by the absorbed photons in photoacoustic microscopy," Optics Letters **35** (23), 4018.

Zhang, Xiangyang, Hao F. Zhang, and Shuliang Jiao (2012c), "Optical coherence photoacoustic microscopy: accomplishing optical coherence tomography and photoacoustic microscopy with a single light source," Journal of Biomedical Optics **17** (3), 030502.

Zhang, Xiangyang, Hao F. Zhang, Carmen A. Puliafito, and Shuliang Jiao (2011), "Simultaneous in vivo imaging of melanin and lipofuscin in the retina with photoacoustic ophthalmoscopy and autofluorescence imaging," Journal of Biomedical Optics **16** (8), 080504.

Zhang, Zhen, Biqin Dong, Hao Li, Fan Zhou, Hao F. Zhang, and Cheng Sun (2014), "Theoretical and experimental studies of distance dependent response of micro-ring resonator-based ultrasonic detectors for photoacoustic microscopy," Journal of Applied Physics **116** (14), 144501.

Zhu, Xiaoyi, Zhiyu Huang, Guohe Wang, Wenzhao Li, Da Zou, and Changhui Li (2017), "Ultrasonic detection based on polarization-dependent optical reflection," Optics Letters **42** (3), 439.

Zuomin Zhao,, S. Nissila, O. Ahola, and R. Myllyla (1998), "Production and detection theory of pulsed photoacoustic wave with maximum amplitude and minimum distortion in absorbing liquid," IEEE Transactions on Instrumentation and Measurement **47** (2), 578–583.